SCISPACE
formerly Typeset

Open access • Journal Article • DOI:10.3847/0004-637X/820/2/121

POSSIBLE SIGNATURES of A COLD-FLOW DISK from MUSE USING A z ~ 1 GALAXY-QUASAR PAIR TOWARD SDSS J1422-0001 — Source link

Nicolas Bouché, H. Finley, Ilane Schroetter, Michael T. Murphy ...+22 more authors

Institutions: Hoffmann-La Roche, Centre national de la recherche scientifique, Swinburne University of Technology, University of Potsdam ...+8 more institutions

Published on: 30 Mar 2016 - The Astrophysical Journal (IOP Publishing)

Topics: Galaxy, Quasar, Metallicity and Star formation

Related papers:

- Possible Signatures of a Cold-Flow Disk from MUSE using a z=1 galaxy--quasar pair towards SDSSJ1422-0001
- Signatures of Cool Gas Fueling a Star-Forming Galaxy at Redshift 2.3
- How do galaxies get their gas
- Four phases of angular-momentum buildup in high-z galaxies: from cosmic-web streams through an extended ring to disc and bulge
- Cold streams in early massive hot haloes as the main mode of galaxy formation.

Share this paper:

View more about this paper here: https://typeset.io/papers/possible-signatures-of-a-cold-flow-disk-from-muse-using-a-z-5310j88ej9

The Astrophysical Journal, 820:121 (17pp), 2016 April 1 doi:10.3847/0004-637X/820/2/121
© 2016. The American Astronomical Society. All rights reserved.

POSSIBLE SIGNATURES OF A COLD-FLOW DISK FROM MUSE USING A $z \sim 1$ GALAXY–QUASAR PAIR TOWARD SDSS J1422−0001*

N. Bouché[1], H. Finley[2,3], I. Schroetter[2,3], M. T. Murphy[4], P. Richter[5,6], R. Bacon[7], T. Contini[2,3], J. Richard[7], M. Wendt[5,6], S. Kamann[8], B. Epinat[2,9], S. Cantalupo[10], L. A. Straka[11], J. Schaye[11], C. L. Martin[12], C. Péroux[9], L. Wisotzki[5], K. Soto[10], S. Lilly[10], C. M. Carollo[10], J. Brinchmann[11,13], and W. Kollatschny[8]
[1] CNRS/IRAP, 9 Avenue Colonel Roche, F-31400 Toulouse, France
[2] CNRS/IRAP, 14 Avenue E. Belin, F-31400 Toulouse, France
[3] University Paul Sabatier of Toulouse/UPS-OMP/IRAP, F-31400 Toulouse, France
[4] Centre for Astrophysics and Supercomputing Swinburne University of Technology, Hawthorn, Victoria 3122, Australia
[5] AIP, Leibniz-Institut für Astrophysik Potsdam, An der Sternwarte 16, D-14482 Potsdam, Germany
[6] Institut für Physik und Astronomie, Universität Potsdam, Karl-Liebknecht-Str. 24/25, D-14476 Golm, Germany
[7] Univ. Lyon, Univ. Lyon1, Ens de Lyon, CNRS, Centre de Recherche Astrophysique de Lyon UMR5574, F-69230, Saint-Genis-Laval, France
[8] Institut für Astrophysik, Universität Göttingen, Friedrich-Hund-Platz 1, D-37077 Göttingen, Germany
[9] Aix-Marseille Université, CNRS, LAM (Laboratoire dAstrophysique de Marseille) UMR 7326, F-13388 Marseille, France
[10] ETH Zurich, Institute of Astronomy, Wolfgang-Pauli-Str. 27, 8093 Zurich, Switzerland
[11] Leiden Observatory, Leiden University, P.O. Box 9513, 2300 RA Leiden, The Netherlands
[12] Department of Physics, University of California Santa Barbara, Santa Barbara, CA, USA
[13] Instituto de Astrofísica e Ciências do Espaço, Universidade do Porto, CAUP, Rua das Estrelas, PT4150-762 Porto, Portugal
Received 2015 September 8; accepted 2016 January 22; published 2016 March 30

ABSTRACT

We use a background quasar to detect the presence of circumgalactic gas around a $z = 0.91$ low-mass star-forming galaxy. Data from the new Multi Unit Spectroscopic Explorer (MUSE) on the Very Large Telescope show that the galaxy has a dust-corrected star formation rate (SFR) of $4.7 \pm 2.0\ M_{\odot}\,\mathrm{yr}^{-1}$, with no companion down to $0.22\ M_{\odot}\,\mathrm{yr}^{-1}$ (5σ) within 240 h^{-1} kpc ("30"). Using a high-resolution spectrum of the background quasar, which is fortuitously aligned with the galaxy major axis (with an azimuth angle α of only 15°), we find, in the gas kinematics traced by low-ionization lines, distinct signatures consistent with those expected for a "cold-flow disk" extending at least 12 kpc ($3 \times R_{1/2}$). We estimate the mass accretion rate $\dot{M}_{\rm in}$ to be at least two to three times larger than the SFR, using the geometric constraints from the IFU data and the H I column density of $\log N_{\rm H\,I}/\mathrm{cm}^{-2} \simeq 20.4$ obtained from a *Hubble Space Telescope*/COS near-UV spectrum. From a detailed analysis of the low-ionization lines (e.g., Zn II, Cr II, Ti II, Mn II, Si II), the accreting material appears to be enriched to about $0.4\ Z_{\odot}$ (albeit with large uncertainties: $\log Z/Z_{\odot} = -0.4 \pm 0.4$), which is comparable to the galaxy metallicity ($12 + \log \mathrm{O/H} = 8.7 \pm 0.2$), implying a large recycling fraction from past outflows. Blueshifted Mg II and Fe II absorptions in the galaxy spectrum from the MUSE data reveal the presence of an outflow. The Mg II and Fe II absorption line ratios indicate emission infilling due to scattering processes, but the MUSE data do not show any signs of fluorescent Fe II* emission.

Key words: galaxies: evolution – galaxies: formation – intergalactic medium – quasars: individual (SDSS J142253.31–000149)

1. INTRODUCTION

A number of indirect arguments imply that galaxies are fed by the accretion of intergalactic gas throughout their evolution. For instance, the amount of cold gas present in local and distant galaxies is barely enough to sustain their star formation rates (SFRs) for another Gyr or so (e.g., Leroy et al. 2008; Freundlich et al. 2013; Saintonge et al. 2013; Tacconi et al. 2013). Another indirect argument comes from the metallicity distribution of G stars in the Milky Way, which is not consistent with what one finds with "closed-box" chemical evolution models unless some fresh gas infall is invoked (Lynden-Bell 1975; Pagel & Patchett 1975). This is often referred to as the G-dwarf problem (van den Bergh 1962; Schmidt 1963). The very mild evolution of the cosmic neutral density $\Omega_{\rm H\,I}$ for damped Lyα absorbers (e.g., Péroux et al. 2003; Noterdaeme et al. 2012; Crighton et al. 2015, and references therein), together with the rapid evolution of the stellar cosmic density, is another indirect argument for continuous replenishment of galaxy reservoirs.

In numerical simulations, accretion of intergalactic gas (via the cosmic web) originates from the growth of dark matter halos, which pulls the cold baryons along. In galaxies with luminosities less than L^*, this process is expected to be very efficient owing to the short cooling times in these halos (White & Frenk 1991; Birnboim & Dekel 2003). This process is expected to lead to distinct signatures in absorption systems with $N_{\rm H\,I}$ of 10^{17}–$10^{21}\,\mathrm{cm}^{-2}$ seen in background quasar sightlines (Dekel et al. 2009; Kimm et al. 2011b; Fumagalli et al. 2011, 2014; Stewart et al. 2011a; Goerdt et al. 2012; van de Voort & Schaye 2012). Once inside the galaxy dark matter halo, the accreted gas is expected to orbit the galaxy, delivering not just fuel for star formation but also angular momentum (Stewart et al. 2011a; Danovich et al. 2015). In this context, the accreting material coming from the large-scale filamentary structure should co-rotate with the central disk, forming a

* Based on observations made at the ESO telescopes under program 080.A-0364 (SINFONI), 079.A-0600 (UVES), and as part of MUSE commissioning (ESO program 060.A-9100). Based on observations made with the NASA/ESA *Hubble Space Telescope*, obtained at the Space Telescope Science Institute, which is operated by the Association of Universities for Research in Astronomy, Inc., under NASA contract NAS 5-26555. These observations are associated with program ID 12522.

warped, extended gaseous structure (Kimm et al. 2011a; Pichon et al. 2011; Danovich et al. 2012, 2015; Shen et al. 2013), sometimes referred to as a "cold-flow disk" (Stewart et al. 2011a, 2013). In the local universe, such large gaseous disks are often seen around galaxies in H I 21 cm surveys, where the H I disk extends 2–3 times beyond the stellar radius as in the M33 low surface brightness disk (Putman et al. 2009) and the more massive M81 (Yun et al. 1994) and M83 galaxies (Huchtmeier & Bohnenstengel 1981; Bigiel et al. 2010), among others. The kinematics of this H I gas in the outer parts show that it is systematically rotating in the same direction as the central object.

These gaseous structures ought to produce distinct kinematic signatures in absorption systems, as argued by Stewart et al. (2011a, 2013). The infalling gas kinematics is expected to be offset from the galaxy's systemic velocity when observed in absorption along background quasar sightlines (Stewart et al. 2011a) because the gas is not rotationally supported. These expected signatures are testable against observations with suitably located background sources such as background quasars (Bouché et al. 2013) or background galaxies (Diamond-Stanic et al. 2015).

Bouché et al. (2013) presented a first comparison of such inflow kinematics in a $z \simeq 2.3$ galaxy–quasar pair toward the quasar HE 2243−60. The apparent location of this background quasar (and the one presented in this study) is fortuitously aligned with the galaxy major axis. This configuration is the most favorable situation to look for such inflow kinematic signatures since it removes deprojection ambiguities and the geometry allows us to rule out any outflow interpretation. The data presented in Bouché et al. (2013) showed observational signatures similar to theoretical predictions (Stewart et al. 2011a; Shen et al. 2013; Danovich et al. 2015). If the accreting material coming from the large-scale filamentary structure forms a roughly co-planar structure around the galaxy with an azimuthal symmetry, one can infer the amount of gas involved in the process and hence the accretion rate. The $z \simeq 2.3$ galaxy in Bouché et al. (2013) was found to have an SFR of $\sim 30\ M_\odot\ \mathrm{yr}^{-1}$ and an accretion rate of 30–60 $M_\odot\ \mathrm{yr}^{-1}$.

Other kinematic evidence of gas inflows from redshifted absorption lines in galaxy spectra has been reported by Martin et al. (2012) and Rubin et al. (2012); however, these studies lack the critical information on the spatial location of the infalling material with respect to the host. The recent IFU observations of Martin et al. (2015) of a giant Lyα-emitting filament around a high-redshift quasar (Cantalupo et al. 2014) provide possible evidence for kinematics compatible with a large (220 kpc in radius) gaseous rotating disk.

In this paper, we use a quasar–galaxy pair toward the quasar SDSS J142253.31−000149 (hereafter SDSS J1422−00) to search for the kinematic signatures of gas inflows. This quasar is selected from our SINFONI Mg II Program for Line Emitters (SIMPLE) survey (Bouché et al. 2007, hereafter Paper I). The SIMPLE survey consists of a search for galaxies around strong $z \sim 0.8$–1.0 Mg II absorbers selected from the Sloan Digital Sky Survey (SDSS) database with rest-frame equivalent widths $W_r^{\lambda 2796} > 2$ Å using the IFU SINFONI. In Schroetter et al. (2015, hereafter Paper II), we analyzed the quasar apparent location with respect to the host kinematic axis using our GalPaK^{3D} algorithm (Bouché et al. 2015) and found that this quasar is also fortuitously aligned with the host galaxy's major axis, as in the $z \sim 2$ pair discussed in Bouché et al. (2013), at an impact parameter of 12 kpc (1.″4) from the host. This fortuitous alignment makes this quasar–galaxy pair an excellent candidate to study the properties of cold-flow disks.

In order to test the capabilities of the new Multi Unit Spectroscopic Explorer (MUSE) instrument (Bacon et al. 2006, 2010, 2015) on the Very Large Telescope (VLT), this field was observed during the second commissioning run on 2014 May 06. These observations, covering [O II] and Hβ, complement the Hα+[N II] observations of SINFONI, allowing us to constrain the interstellar medium (ISM) metallicity. We also have a deep high-resolution VLT/UVES (Ultraviolet and Visual Echelle Spectrograph) spectrum of the background quasar and a near-UV (NUV) spectrum obtained with the G230L grating of the Cosmic Origin Spectrograph (COS) on board the *Hubble Space Telescope* (*HST*), allowing us to constrain the metallicity of the absorbing material. Furthermore, the UVES kinematics yield insights into the physical nature of the gas and show similar features to those in the hydrosimulations of Stewart et al. (2011a) and Shen et al. (2013).

In Section 2, we present the observations obtained with the VLT/MUSE instrument (Section 2.1) and the *HST*/COS spectra (Section 2.2). In Section 3, we present ancillary SINFONI and UVES data obtained on this quasar–galaxy pair. In Section 4, we present the analysis of the IFU data at hand (MUSE and SINFONI), with respect to the host galaxy, namely, its SFR and its emission kinematics. In Section 5, we present the analysis of the properties of the circumgalactic gas. Throughout this paper, we use the standard ΛCDM cosmology with the parameters $\Omega_m = 0.3$, $\Omega_\Lambda = 0.7$, and a Hubble constant $H_0 = 100\,h$ km s^{-1} Mpc^{-1} with $h = 0.7$.

2. NEW OBSERVATIONS

2.1. VLT/MUSE

This $z = 1.08$ quasar was observed with the new wide-field ($1' \times 1'$) IFU for the VLTs (MUSE; Bacon et al. 2010) during the second commissioning run on 2014 May 6 under good seeing conditions (FWHM $\sim 0.''6$) for 2 hr, in 4×30 minute exposures (Table 1). The data were reduced with the MUSE pipeline[13] v1.0 with standard settings. We used the bias, flat-field calibrations, and arc lamp exposures taken during the day for that night. The wavelength solution is calibrated on the air scale. To minimize flat-field errors from spatial shifts related to temperature changes during the night, we only use the flat fields that were taken when the temperature was within ±0.5°C from the ambient temperature of the observations (mean of 15.1°C). We used four twilight flats, each rotated at 90°, and corrected for vignetting using the vignetting mask. With these calibrations, we processed the raw science data using the MUSE recipes *scibasic* and *scipost* with the sky removal option turned off to produce data cubes and pixel tables for each of the four exposures.

The individual exposures were registered using the point sources in the field, ensuring accurate relative astrometry, as significant shifts of a few tens of arcsecs can occur owing to the spatial shifts introduced by the derotator wobble between exposures. The pixel tables from the individual exposures were then combined to a single data cube produced using a 3D drizzle interpolation process. The MUSE data cube is sampled

[13] A short description of the pipeline is given in Weilbacher et al. (2012).

Table 1
Observation Summary

Instrument	Setting	T_{exp}	PSF	Date of Observation
VLT/UVES	390 + 564	9000 s	1.″0	2007 Apr. 12, 14
VLT/ SINFONI	J250	9600 s	0.″8	2008 Feb. 15, 25 2008 Mar. 14
VLT/MUSE	WFM-NOAO-N	7200 s	0.″6	2014 May 06
HST/COS	G230L	11290 s	…	2013 Jan. 25

Note. For each instrument we show the setting used, the exposure time, the point-spread function (PSF) FWHM, and the dates of the observations.

to a common grid (0.″2 × 0.″2 × 1.25 Å), and the final wavelength solution is calibrated on air and corrected for the heliocentric velocity. The cube is available at this URL: http://muse-vlt.eu/science/j1422.

We checked the wavelength solution against the wavelength of OH lines and found it to be accurate within 10 km s^{-1}. We forced the final astrometry solution to match the SDSS coordinates using the point sources in the field. The sky subtraction was performed on the combined exposure with the Zurich Atmospheric Purge (ZAP) principal component algorithm developed by K. T. Soto et al. (2016, in preparation), which was designed to remove OH line residuals. The flux calibration was obtained from observations of the spectrophotometric standard star GD 108. The night was photometric, and we cross-checked the flux measurements against the SDSS magnitudes by fitting a Moffat function to the stars in the field in reconstructed images obtained with the SDSS filter curves. We found no difference between the SDSS magnitudes and our measurements greater than 0.01 mag.

From the noise in the data at the expected wavelength of [O II] (∼7118 Å), 2.3 × 10^{-20} erg s^{-1} cm^{-2} Å^{-1} (1σ) per pixel, we estimate a surface brightness limit of 1.5 × 10^{-18} erg s^{-1} cm^{-2} arcsec^{-2} (1σ) for emission-line objects (FWHM = 2.14 × 1.25 Å), which corresponds to a flux limit of 6 × 10^{-19} erg s^{-1} cm^{-2} (1σ) for unresolved line emitters at 0.″7 seeing. For the [O II] doublet, the flux limit is twice this value, or ∼1.2 × 10^{-18} erg s^{-1} cm^{-2} (1σ). Hence, our 5σ limit for unresolved [O II] emitters at $z \approx 0.91$ corresponds to an SFR of 0.22 $M_{\odot}$ yr^{-1} using the Kewley et al. (2004) calibration with no dust reddening (as in Section 4.3). The flux limit for an unresolved continuum emission (3 × 3 spaxel) is ∼8 × 10^{-20} erg s^{-1} cm^{-2} Å^{-1} (1σ), corresponding to ∼25.8 (24.7; 3σ) AB magnitudes at 7100 Å. Note that the MUSE sensitivity is weakly dependent on wavelength, outside regions affected by sky emission lines.

Figure 1 shows the MUSE data, with a color image made from three broadband images (V, R, and I) extracted from the data cube. The quasar location is represented by the cross. For completeness, we have searched for all galaxies using both a visual inspection of the cube and a SExtractor-based algorithm (muselet; J. Richard et al., in preparation), and we found 41 galaxies with emission or absorption lines, of which 37 have a reliable redshift. The coordinates and redshifts of these galaxies are listed in Table 2, and their locations are shown in Figure 1 with the redshifts labeled.

Here we are only interested in galaxies with redshifts comparable to the Mg II absorption redshifts at $z \approx 0.91$, and the MUSE field of view (1′× 1′) allows us to investigate whether the Mg II absorption could be associated with other host galaxies that would have fallen outside the SINFONI field of view (8″ × 8″). Figure 2 shows a pseudo-narrowband image centered on the expected [O II] wavelength of 7110–7120 Å (8 spectral pixels) with a linear continuum subtraction from the MUSE data, where the quasar SDSS J1422−00 is marked by the cross and black circle. Only two [O II] emitters are detected, one at an impact parameter of only $b = 1.″45$ (∼12 kpc) and another at 40.″5 (∼315 kpc) in the NW corner of the field. The second one is at a large distance (about 3.3 × R_{vir}), implying that it is likely unrelated to the absorbing gas. There are no other [O II] emitters within ±5000 km s^{-1} down to 0.22 $M_{\odot}$ yr^{-1} (5σ), and the objects visible in white correspond to imperfect continuum subtraction of stellar objects with strong continuum slopes.

2.2. HST/COS

In order to characterize the H I gas column density probed by the background quasar, we obtained a spectrum of the quasar with the NUV G230L grating of the *HST*/COS instrument (Cycle 19, program ID 12522; PI: N. Bouché) covering the Lyα λ1216 transition at $\lambda_{obs} = 2321$ Å. The *HST*/COS spectrum was obtained on 2013 January with four orbits for a total exposure time of $T_{exp} = 11,290$ s (Table 1). The spectrum has a resolution of $R \sim 2900$ In the wavelength range 2100–2550 Å of stripe A of the G230L grating. The final spectrum was reduced with the COS *calcos* (Kaiser et al. 2008) pipeline and has a signal-to-noise ratio (S/N) of ∼3 around the wavelength of the redshifted Lyα absorption line.

3. ANCILLARY DATA

3.1. VLT/SINFONI

The original VLT/SINFONI data covering the quasar J1422 −00 (Paper I) revealed the host galaxy at $z = 0.9096 \pm 0.0001$ in shallow (40-minute integration time) exposures. We reobserved the field with SINFONI for 2.6 hr in 2008 (Table 1). In Paper II, we presented the analysis of these VLT/SINFONI data of this field along with the 13 other quasar fields making the SIMPLE sample. The data reduction was performed as in Paper I and Förster Schreiber et al. (2009), using the SINFONI pipeline (SPRED; Schreiber et al. 2004; Abuter et al. 2006) and complemented with custom routines for OH sky-line removal (Davies 2007) and using the Laplacian edge cosmic-ray removal technique of van Dokkum (2001). The SINFONI data cube is sampled at 0.″125 × 0.″125 × 1.4 Å, and the wavelengths are calibrated on the vacuum scale.

3.2. VLT/UVES

As part of the SIMPLE survey, the quasar was observed with the high-resolution VLT/UVES spectrograph. The VLT/UVES data were taken with the 390 + 564 nm central wavelength setting. The data were reduced using version 3.4.5 of the UVES pipeline in MIDAS, and the data reduction details were presented in Paper II.

4. HOST GALAXY PROPERTIES

4.1. QSO PSF Subtraction

Given the small impact parameter (1.″4), the quasar continuum emission overlaps spatially with the Mg ii absorber

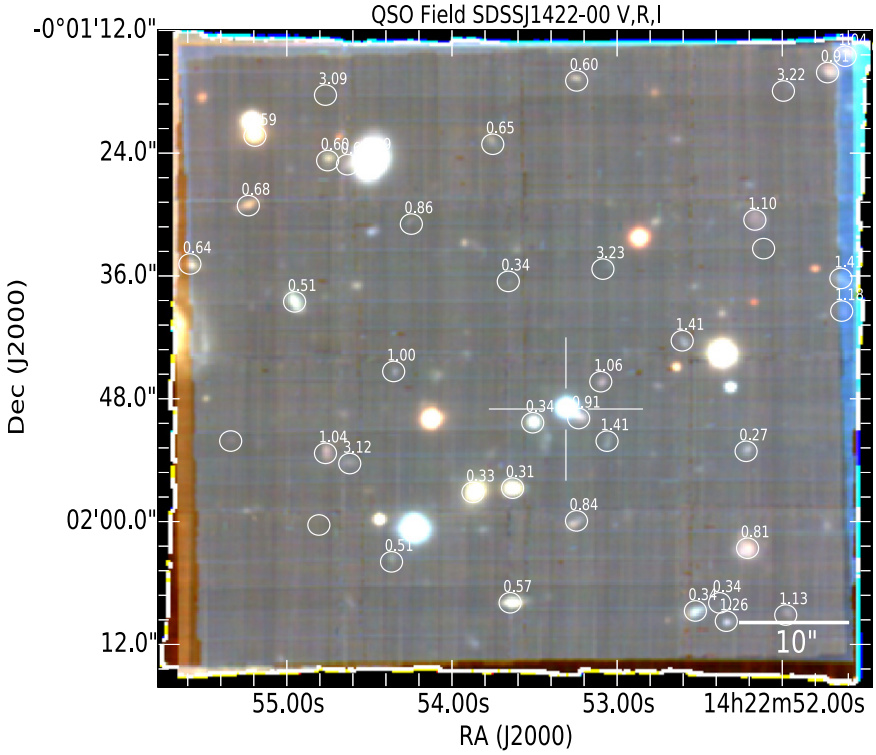

Figure 1. Color image made from three broadband images (V, R, and I) extracted from the MUSE data cube showing the entire $1' \times 1'$ field of view. The QSO location is indicated by the cross. Galaxies with secure redshifts are labeled with white circles. Circles with no label indicate that an emission line is present, but the redshift identification is not secure. Table 2 lists all of the sources found in the field.

galaxy emission (see Figure 2). We therefore need to carefully remove the quasar continuum in the MUSE data before performing any detailed kinematic analysis. The continuum subtraction task is complicated by an [Ne v] λ3425 emission from the QSO, which appears at around the same wavelength (7115 Å) as the [O ii] $\lambda\lambda$3727, 3729 doublet from the host galaxy.

To remove the QSO continuum that overlaps with the [O ii] emitter, we constructed a 3D PSF using the PampelMuse algorithm (Kamann et al. 2013) to interactively and simultaneously fit the QSO continuum and the PSF. We then removed this 3D PSF from the cube. The resulting narrowband image is shown in the top right subpanel of Figure 2. The other two subpanels in Figure 2 show three spectra taken at the three positions labeled in the first inset before (middle) and after (bottom) the 3D PSF subtraction. These spectra show that the [O ii] emission in the overlap region ("2") becomes clearly apparent after the PSF subtraction.

4.2. Host Galaxy Redshift

Much of the analysis presented in the following sections depends on the redshift of the host and its accuracy. Therefore, we use several methods to cross-check our measurements and remove possible systematic errors. As in Paper II, we determine the redshift from the mean wavelength of the reddest and the bluest parts of the [O ii] emission (along the kinematic major axis) and from a pseudo-long slit aligned with the kinematic major axis. We also estimated the redshift from Hα in the SINFONI data using a similar technique and found $z \simeq 0.9096$ (Paper II).

Figure 3 shows the pseudo-long slit two-dimensional spectra extracted from the MUSE QSO-subtracted data cube with a $1''$ slit passing through the location of the QSO and the galaxy. The continuum trace of the galaxy is visible at an impact parameter of $\sim 1''.45$ (12 kpc) and is marked by the horizontal line. The best redshift from the [O ii] MUSE data is estimated from the reddest [O ii] component (λ3728.8), whose kinematic center appears to be at 7120.5 Å, corresponding to 0.9096 ± 0.0001. The global kinematic fit discussed in the next section yields a redshift consistent with this value.

Hence, we adopt a systemic redshift of the Mg ii host galaxy of 0.9096 ± 0.0001.

4.3. Fluxes, SFR

Our VLT/SINFONI data toward the $z_{\rm qso} = 1.083$ quasar SDSS J1422−00 already revealed the host galaxy of the strong Mg ii absorber with $W_{\rm r}^{\lambda 2796} = 3.2$ Å at $z \simeq 0.9096$ (Papers I, II), whose Hα flux of $(9.0 \pm 0.1) \times 10^{-17}$ erg s^{-1} cm^{-2} corresponds to an observed SFR$_{\rm H\alpha}$ of $2.8 \pm 0.2\ M_\odot\ {\rm yr}^{-1}$ assuming a Salpeter initial mass function (IMF) from 0.1 to 100 $M_\odot$ and applying no dust correction. With an extinction of $E(B-V) = 0.1$ (see below), the intrinsic SFR is found to be $3.5 \pm 0.2\ M_\odot\ {\rm yr}^{-1}$. The SINFONI data did not reach the sensitivity required to detect the [N ii] emission, but our data did allow us to obtain a 2σ upper limit of $f_{\rm N\,II} < 3 \times 10^{-17}$ erg s^{-1} cm^{-2}.

From the VLT/MUSE data, we find (top two panels in Figure 4) that the [O ii] flux is $(1.1 \pm 0.2) \times 10^{-17}$ erg s^{-1} cm^{-2} and the Hβ flux is $(3.3 \pm 0.3) \times 10^{-17}$ erg s^{-1} cm^{-2}. We do not detect [O iii] λ4363, which leads to a 2σ upper limit of $<1 \times 10^{-18}$ erg s^{-1} cm^{-2}. These total flux measurements (summarized in Table 3) were obtained from the global 3D line fitting to the MUSE data described in the next section (Section 4.5). We also used the traditional "growth

Table 2
MUSE Sources in the SDSS J1422−00 Field

ID	R.A.	Decl.	Redshift	Lines
obj029	14:22:51.619	−00:01:14.53	⋯	7619
obj042	14:22:51.640	−00:01:39.43	1.176	[O II]
obj035	14:22:51.645	−00:01:36.24	1.406	[O II]
obj028	14:22:51.726	−00:01:16.13	0.909	[O II]
obj033	14:22:51.979	−00:02:09.13	1.130	[O II]
obj006	14:22:51.993	−00:01:17.93	3.224	Lyα
obj008	14:22:52.113	−00:01:33.33	⋯	5160.
obj032	14:22:52.166	−00:01:30.53	1.100	[O II]
obj039	14:22:52.219	−00:01:53.13	0.266	[O III], Hβ
obj023	14:22:52.233	−00:02:02.33	0.811	[O II], [O III], Hβ
obj034	14:22:52.339	−00:02:09.73	1.259	[O II]
obj003	14:22:52.379	−00:02:07.94	0.345	Hα, Hβ, [O III], [O II]
obj004	14:22:52.526	−00:02:08.73	0.345	Hα, Hβ, [O III], [O II]
obj036	14:22:52.606	−00:01:42.33	1.405	[O II]
obj037	14:22:53.061	−00:01:52.14	1.407	[O II]
obj007	14:22:53.086	−00:01:35.33	3.227	Lyα
obj031	14:22:53.099	−00:01:46.33	1.059	[O II]
obj027	14:22:53.233	−00:01:49.93	0.909	[O II]
obj014	14:22:53.245	−00:01:16.94	0.600	[O II], [O III], Hβ
obj024	14:22:53.246	−00:01:59.93	0.839	[O II], [O III], Hβ
obj002	14:22:53.511	−00:01:50.34	0.345	Hα, [N II], [O III], Hβ, [O II]
obj019	14:22:53.633	−00:01:56.73	0.309	CaHK
obj011	14:22:53.659	−00:02:07.93	0.575	[O II], [O III], Hβ, Hg...
obj022	14:22:53.659	−00:01:36.53	0.340	[O III], Hβ,
obj015	14:22:53.753	−00:01:23.13	0.652	[O II], [O III]
obj018	14:22:53.873	−00:01:57.14	0.334	CaHK
obj025	14:22:54.246	−00:01:30.93	0.859	[O II]
obj038	14:22:54.353	−00:01:45.33	0.996	[O II]
obj026	14:22:54.366	−00:02:03.93	0.512	[O II], [O III], Hβ
obj001	14:22:54.499	−00:01:24.74	0.188	Hα, [S II], [N II], [O III]
obj005	14:22:54.619	−00:01:54.33	3.122	Lyα
obj021	14:22:54.633	−00:01:25.13	0.676	[O II], [O III], Hβ
obj012	14:22:54.753	−00:01:24.73	0.600	[O II], [O III], Hβ
obj016	14:22:54.766	−00:01:18.33	3.086	Lyα
obj030	14:22:54.766	−00:01:53.33	1.043	[O II]
obj009	14:22:54.806	−00:02:00.33	⋯	5528.
obj010	14:22:54.953	−00:01:38.53	0.513	[O II], [O III], Hβ, Hg...
obj017	14:22:55.193	−00:01:22.33	0.588	CaHK
obj020	14:22:55.233	−00:01:29.13	0.675	[O II], CaHK
obj040	14:22:55.587	−00:01:34.83	0.641	[O II], [O III]
obj041	14:22:55.340	−00:01:52.13	⋯	8438

Note. For each source, we list the J2000 coordinates, the redshift, and the line (s) used in securing the redshift. When the line is unique or its shape ambiguous, we list the observed wavelength in Å.

curve" technique to verify these values. The [O II] luminosity corresponds to an $SFR_{[O\,II]}$ of $3.0 \pm 0.1\ M_\odot\,yr^{-1}$ using the revised calibration of Kewley et al. (2004), which makes no assumption about reddening.

Taking the Hα and Hβ fluxes at face value, i.e., ignoring possible systematics in the flux calibration between MUSE (accurate to 0.01 mag) and SINFONI (accurate to 0.15 mag or 15%), the extinction is $E(B-V) = 0.1 \pm 0.1$ from the Balmer decrement. Using the Balmer decrement for the reddening, the extinction at [O II] is 0.5 mag, yielding an intrinsic SFR (SFR_0) of around $4.7 \pm 2.0\ M_\odot\,yr^{-1}$ for a Salpeter IMF ranging from 0.1 to 100 $M_\odot$.[14] The flux ratio [O II]/Hα (≈1) and our low dust estimate are entirely consistent with the observations of local galaxies from Sobral et al. (2012) and Kewley et al. (2004), which showed that the [O II]/Hα ratio is strongly dependent on the Balmer decrement, with [O II]/Hα around ∼1 where the Balmer decrement Hα/Hβ is ∼3, as in our data.

Hence, the SFR estimates from Hα and [O II] are consistent with each other, and we adopt an SFR of $4.7 \pm 2.0\ M_\odot\,yr^{-1}$ for a Chabrier (2003) IMF. Table 4 summarizes the extinction and SFR measurements. Using the galaxy half-light radius of $R_{1/2} = 4.0 \pm 0.2$ kpc found in Section 4.5, the SFR surface density is $\Sigma_{SFR} \simeq 0.05 \pm 0.02\ \ M_\odot\,yr^{-1}\,kpc^{-2}$, where the uncertainty is dominated by the SFR uncertainties.

4.4. Metallicity

From the nebular line ratios, [N II]/Hα and [O II]/Hβ (Table 3), we can constrain the galaxy metallicity. Figure 5 shows the likelihood contours allowed by the data from the [N II]/Hα and [O II]/Hβ measurements, yielding an extinction consistent with zero. This is driven by the [O II]/Hβ ratio being already above the maximum value between [O II]/Hβ and metallicity (e.g., Maiolino et al. 2008), and any dust reddening will increase this ratio further, implying that the global fit yields no additional constraint on dust reddening. In the previous section, we argued that $E(B-V) \simeq 0.1$ from the Balmer decrement, which is shown by the white circle in Figure 5. Hence, the relation between the [O II]/Hβ ratio and metallicity imposes a metallicity $12 + \log O/H = 8.7 \pm 0.2$, regardless of the extinction value,[15] at the peak of the relation between [O II]/Hβ and metallicity. Hence, the metallicity estimate is robust against the reddening estimate as illustrated by the contours in Figure 5. Systematic uncertainty remains in the metallicity absolute calibration, as the metallicity might depend on the N/O abundances, as argued by Pérez-Montero & Contini (2009) and Pérez-Montero et al. (2013). We conclude that the ISM of this galaxy is enriched at a metallicity $\log Z/Z_\odot = 0.0 \pm 0.2$ using the solar value $12 + \log O/H = 8.7$ for oxygen (Asplund et al. 2009).

Spatial variations of the [O II]/Hβ flux ratio might indicate the presence of a metallicity gradient. However, the weaker Hβ line has a smaller S/N than [O II] and falls at 9280 Å, close to the end of the wavelength coverage of MUSE, where the MUSE sensitivity drops sharply. Given the difficulty in mapping the Hβ line in this part of the spectrum, we fitted [O II] and Hβ jointly with the CAMEL algorithm of Epinat et al. (2012). The resulting [O II]/Hβ map shows no variations along the galaxy major axis, but shows a possible gradient along the galaxy minor axis: the ratio increases from 2.3 ± 0.1 in the center to 3.0–4.0 at the edges. This could be due to variations in ionization conditions or to systematic errors from the weaker Hβ line, which also appears to be more compact (Table 5).

[14] The SFR_0 would be $\approx 5.0 M_\odot\,yr^{-1}$ using the original Kennicutt (1998) calibration, which includes a dust correction.

[15] Our dust-corrected fluxes with the calibration of Pérez-Montero (2014) yield a metallicity of $12 + \log O/H = 8.5 \pm 0.2$, consistent within the errors with our value, and $\log(N/O) = -1.3 \pm 0.3$. Using our upper limit on [N II] and [O II], we find an upper limit on the $\log(N/O)$ ratio of < -0.9 using the Pérez-Montero & Contini (2009) calibration.

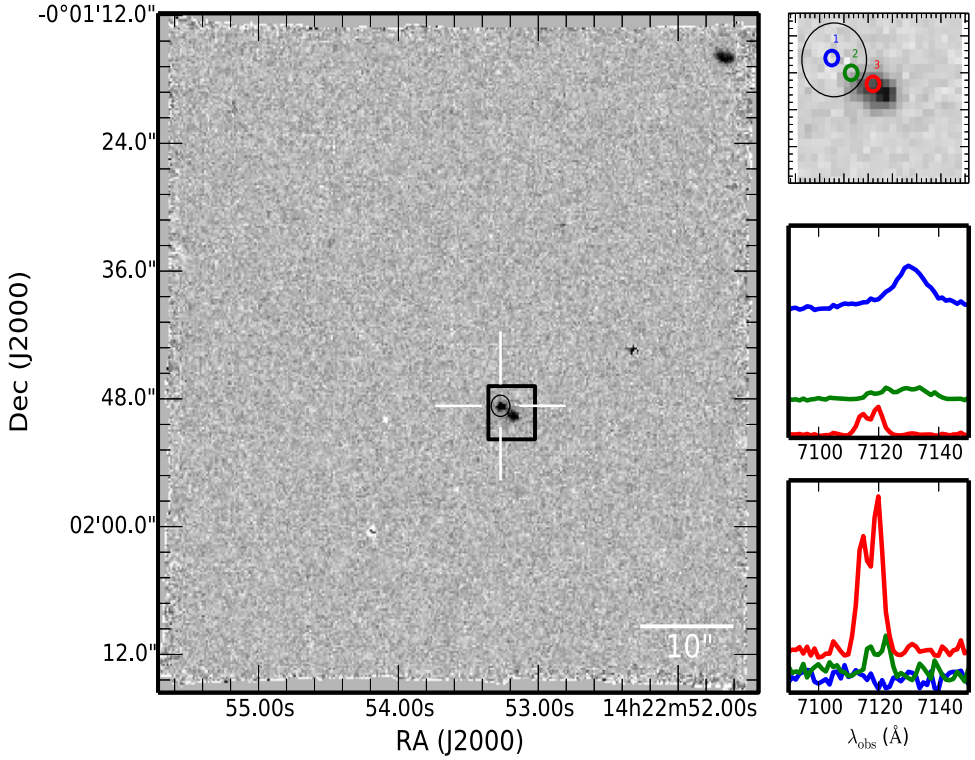

Figure 2. Pseudo-narrowband image (7110–7120 Å) of the MUSE field made at the expected wavelength of [O II] for the redshift ($z \sim 0.9096 \pm 0.0001$) of the strong Mg II absorber with $W_r^{\lambda 2796} = 3.2$ Å. The quasar location is marked by the black circle, which has a radius of 1″. There are two [O II] emitters, one at an impact parameter of 12 kpc (1.″4) and another at an impact parameter of 315 kpc (40.″5) in the NW corner. The faint feature to the west of the quasar is merely residuals from the continuum subtraction of a star. The 5″ × 5″ black square box represents the subfield that will be used in Figure 6 and in the top inset. The top subpanel shows a narrowband image (7110–7120 Å) with the QSO PSF removed (see the text for the details). The middle subpanel shows the spectra around [O II] at the three labeled positions prior to the QSO PSF subtraction, revealing the [Ne V] λ3425 emission from the QSO. The bottom subpanel shows the spectra around [O II] at the three labeled positions after the QSO PSF subtraction. The three spectra (blue, green, and red) are from the three positions labeled 1–3 in the top inset, corresponding to the quasar location ("1"), the overlap region ("2"), and the center of the galaxy ("3").

4.5. Galaxy Kinematics

In Figure 6, we compare the kinematic properties of the host derived from Hα obtained with SINFONI (top two rows) to those derived from [O II] obtained with MUSE (bottom two rows). In this figure, the flux, velocity, and dispersion maps are determined using the two-dimensional line-fitting algorithm LINEFIT and CAMEL for the Hα and [O II] data that are described in Cresci et al. (2009) and Epinat et al. (2012), respectively. CAMEL allows one to fit the two components of the [O II] doublet simultaneously. This figure already shows that the kinematics extracted from Hα and [O II] are consistent with each other, and that the azimuthal angle of the quasar apparent location α is ∼15° from the galaxy P.A.

In order to derive the kinematic parameters, we use the GalPaK^{3D} (v1.6.0) algorithm (Bouché et al. 2015) to fit directly the 3D data using small subcubes around Hα (SINFONI), [O II], and Hβ (MUSE) after removing the galaxy continuum emission using a linear fit. This algorithm fits a 3D parametric disk model to the emission-line data cube and returns the best-fit values for each of the parameters. The algorithm takes into account the PSF and the instrument line-spread function and thus returns the intrinsic ("deconvolved") galaxy properties, such as half-light radius ($R_{1/2}$), total flux (f_{tot}), inclination (i), maximum rotation velocity (V_{max}), and disk velocity dispersion (σ). As described extensively in Bouché et al. (2015), it is particularly well suited for extended objects when the size-to-seeing ratio is 0.5–1.0 or greater.

Here, since $R_{1/2}$ is about 0.″5 and the seeing conditions are ∼0.″8 for SINFONI and ∼0.″6 for MUSE, the size-to-seeing ratio is 0.65–0.9. Hence, because it is close to the formal margin of ∼0.75, it is particularly important to compare the kinematic results of SINFONI with those obtained with MUSE at higher spatial resolution.

To model the galaxy, we used an exponential flux profile $I(r)$, i.e., with a Sérsic index $n = 1$, and an arctangent rotation curve $v(r) \propto \arctan(r/r_t)$, where r_t is the turnover radius. The output parameters do not change when we instead use a Gaussian flux profile. Figure 6 shows the results of the 3D fits to the data with the GalPaK^{3D} algorithm, where we show flux, velocity, and dispersion maps extracted from the modeled data cube, *convolved* with PSF and instrument resolution, for comparison purposes. The values for the morphological and kinematic parameters are listed in Table 5.

From the Hα SINFONI data, as described in Schroetter et al. (2015), the inclination (i) and half-light radius $R_{1/2}$ are well constrained and found to be $i \approx 60°$ and $R_{1/2} \approx 4$ kpc, regardless of the choice in the Sérsic index.

For the [O II] MUSE data, we fit both lines of the [O II] doublet at once, with a unique line ratio of 0.75.[16] We found again the inclination (i) and half-light radius $R_{1/2}$ to be well constrained at $i \approx 60°$ and $R_{1/2} \approx 4$ kpc, regardless of the choice in the Sérsic index n. In other words, the morphological

[16] A map of the line ratios performed by the line-fitting algorithm reveals that it varies slightly from 0.65 to 0.85, i.e., by no more than 15%.

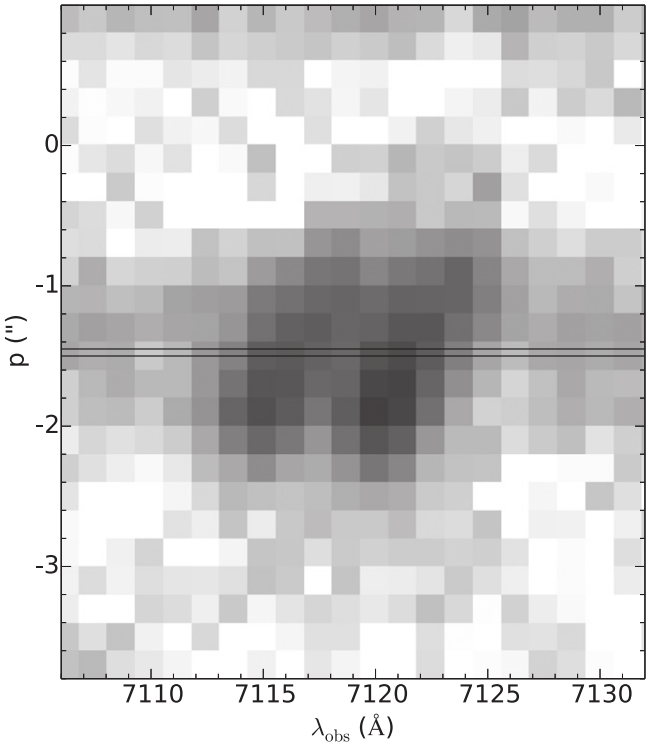

Figure 3. Position–velocity (p–v) diagram extracted from the MUSE data along a pseudo-long slit spectrum around the [O II] emission line covering both the QSO and galaxy location (PA = 55°) where the QSO PSF was subtracted as described in Section 4.1. The QSO trace position is at $y = 0$, and the galaxy trace is seen at an impact parameter of ∼1.″4 (12 kpc). For the reddest transition of the [O II] doublet, at $\lambda_{rest} = 3728.8$ Å, the galaxy systemic velocity is found at ∼7120.5 Å, corresponding to $z = 0.9096 \pm 0.0001$.

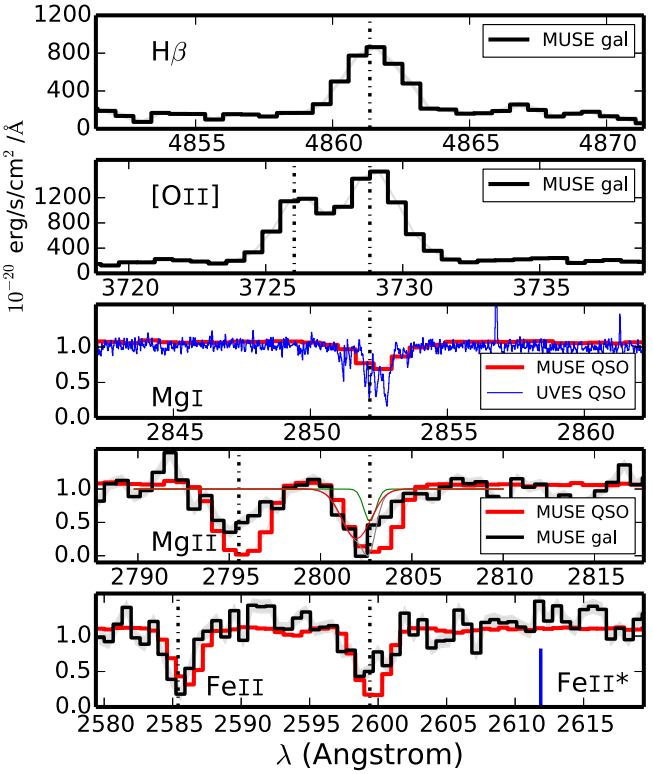

Figure 4. MUSE spectrum. The black solid lines show the galaxy spectrum extracted from the MUSE data cube in a circular aperture of 0.″6 in radius. The red solid lines show the background quasar spectra extracted from the MUSE data cube in a circular aperture with radius 0.″6. The panels show the Hβ and [O II] emission and the Mg I, Mg II, and Fe II absorption from top to bottom respectively. In all panels, the systemic redshift (0.9096 ± 0.0001; see text) is represented by the vertical dotted line. The UVES quasar spectrum for Mg I is shown for comparison in the middle Mg I panel, after converting the UVES spectra to air wavelengths. The Mg I and Mg II absorptions in the background quasar are redshifted with respect to the galaxy systemic velocity. A two-component fit (see Section 4.6) reveals that the Mg II absorption in the galaxy spectrum (second panel from bottom) is blueshifted by $v_{out} \simeq -80 \pm 15$ km s^{-1} with respect to the systemic velocity shown by the vertical dotted line, with a tail up to -150 km s^{-1}. The Fe II λλ2587, 2600 absorption (bottom panel) is consistent with the Mg II profile. The line ratios of the Fe II and Mg II doublets support the presence of infilling emission, but the MUSE spectrum does not reveal any signs for fluorescent Fe II* emission as discussed in Section 4.6.

parameters derived from [O II] are in good agreement with the Hα-derived values.

Regarding the kinematic parameters, we found that the turnover radius r_t is degenerate with the maximum rotation velocity, as already noted in Schroetter et al. (2015) from the Hα data. Hence, we set the turnover radius r_t to 1.5 kpc (∼1 spaxel), to satisfy the scaling relation between r_t and the disk exponential R_d found in local disk samples (Amorisco & Bertin 2010), which is approximately $r_t \simeq R_d \times 0.9$. For fixed turnover radii r_t= 1–2 kpc, we found that the maximum circular velocity V_{max} is 100–110 km s^{-1} for [O II] and around ∼120 km s^{-1} for Hα. The intrinsic velocity dispersion is found to be 30–40 km s^{-1}. The other kinematic and morphological parameters determined from SINFONI and MUSE are listed in Table 5.

We also applied the algorithm to the Hβ MUSE data (shown in Figure 4). The values of the morpho-kinematic parameters derived from the Hβ line are somewhat different (Table 5), with the half-light radius $R_{1/2}$ and V_{max} parameters being somewhat smaller. This is likely due to the fact that the Hβ line lies at 9280 Å, which is at the far end of the MUSE spectral range (9300 Å), where the throughput is much lower. Underlying interstellar absorption in the Hβ profile may also play a role.[17]

From the galaxy size and maximum velocity, we estimate its dynamical mass within its half-light radius to be $M_{dyn}(r < R_{1/2}) \equiv R_{1/2} V^2_{max}/G \approx (2 \pm 0.4) \times 10^{10}$ $M_\odot$. Its halo mass M_h is estimated to be $M_h \approx (1.9 \pm 1.5) \times 10^{11} M_\odot$ using

$$M_h \approx 2 \times 10^{11}\, V^3_{max,100}\, (1+z)^{-1.5}_{1.909} M_\odot, \quad (1)$$

where $V_{max,100}$ is the maximum rotation velocity in units of 100 km s^{-1}, and the redshift factor $1 + z$ is normalized to 1.909. The corresponding halo virial radius $R_{vir} = V_{max}/10/H(z)$ is $R_{vir} \sim 90\, V_{max,110}$ kpc, assuming $V_{vir} = V_{max}$.

4.6. Wind

In this last subsection, we return to Figure 4, where the MUSE host galaxy spectra showed self-absorbed Mg II λλ2796, 2803 components. This Mg II λλ2796, 2803 component is blueshifted with respect to the galaxy systemic velocity, which is most easily explained by a wind being launched from the galaxy (as in Weiner et al. 2009; Erb et al. 2012; Martin et al. 2012; Bordoloi et al. 2014; Chisholm

[17] Note that Hα interstellar absorption equivalent width is much smaller than that of Hβ.

Table 3
Host Galaxy Emission and Absorption Lines

Line	Flux ($erg\ s^{-1}\ cm^{-2}$)	Instrument
$f_{H\alpha,6564}$	$(9.0 \pm 0.1) \times 10^{-17}$	VLT/SINFONI
$f_{N\ II,6583}$	$<3 \times 10^{-17}$ (2σ)	VLT/SINFONI
$f_{O\ II,3727}$	$(1.1 \pm 0.2) \times 10^{-16}$	VLT/MUSE
$f_{H\beta,4861}$	$(3.3 \pm 0.3) \times 10^{-17}$	VLT/MUSE
$f_{O\ III,4363}$	$<1 \times 10^{-18}$ (2σ)	VLT/MUSE
	W_r (Å)	
Mg II λ2796	3.5 ± 0.4	VLT/MUSE
Mg II λ2803	3.7 ± 0.4	VLT/MUSE
Mg II λ2587	2.5 ± 0.4	VLT/MUSE
Fe II λ2600	3.9 ± 0.4	VLT/MUSE
Fe II* λ2612	<0.8 (2σ)	VLT/MUSE
Fe II* λ2626	<0.8 (2σ)	VLT/MUSE
Fe II* λ2632	<0.8 (2σ)	VLT/MUSE

Table 4
Geometry and Galaxy Derived Properties

Parameter	Value
Quasar b (kpc)	12 (1.″4)
gal-qso P.A. (°)	56 ± 2
gal. P.A. (°)	71 ± 3
α (°)	15 ± 2
gal. incl. (°)	60 ± 2
$E(B-V)$	0.1 ± 0.1[a]
SFR $_{H\alpha,obs}$ $(M_\odot\ yr^{-1})$	2.8 ± 0.2[b]
SFR $_{H\alpha,0}$ $(M_\odot\ yr^{-1})$	3.5 ± 2.0[c]
SFR $_{O\ II,obs}$ $(M_\odot\ yr^{-1})$	3.0 ± 0.2[b]
$SFR_{O\ II,0}$ $(M_\odot\ yr^{-1})$	4.7 ± 2.0[c]
$SFR_{O\ II,0}$ $(M_\odot\ yr^{-1})$	2.5 ± 1.0[d]
Σ_{SFR} $(M_\odot\ kpc^{-2})$	0.05
log (N/O)	-1.3 ± 0.3[e] (<-0.9)[f]
12 + log (O/H)	8.7 ± 0.2[g]
$R_{1/2}$ (kpc)	4 ± 0.2
R_{vir} (kpc)	90 ± 5
V_{max} $(km\ s^{-1})$	110 ± 10
M_{dyn} $(<R_{1/2})$ $(10^{10} M_\odot)$	2 ± 0.4
M_h $(10^{11} M_\odot)$	1.9 ± 0.5
M_{bar} $(10^{10} M_\odot)$	0.5 ± 0.1
λ_{gal}	0.04
V_{wind} $(km\ s^{-1})$	100–150
$\dot{M}_{wind}$ $(M_\odot\ yr^{-1})$	0.5–5
R_{in} (kpc)	$\geqslant 12$
V_{in} $(km\ s^{-1})$	≈ 100
$\dot{M}_{in}$ $(M_\odot\ yr^{-1})$	≈ 10
λ_{cfd}	>0.06

Notes.
[a] From the $H\beta/H\alpha$ flux ratio.
[b] For a Salpeter IMF from 0.1 to 100 $M_\odot$.
[c] For a Salpeter IMF from 0.1 to 100 $M_\odot$ with $E(B-V) = 0.1$.
[d] For a Chabrier (2003) IMF from 0.1 to 100 $M_\odot$ with $E(B-V) = 0.1$.
[e] From Pérez-Montero (2014).
[f] Using [N II]/[O II] from Pérez-Montero & Contini (2009).
[g] Using [O II]/Hβ from Maiolino et al. (2008).

et al. 2015; Rubin et al. 2014; Heckman et al. 2015; Wood et al. 2015, among others).

Our MUSE data also show indirect indications of Mg II and Fe II emission. Indeed, the second panel of Figure 4 shows clearly that the Mg II λ2796 optical depth is lower than the Mg II λ2803 transition, a situation opposite from the expected oscillator strengths, which are 0.6 and 0.3, respectively. This is likely the result of Mg II emission infill as proposed by Prochaska et al. (2011) and Scarlata & Panagia (2015) and discussed in Erb et al. (2012). Our MUSE data also show the presence of Fe II $\lambda\lambda$2587, 2600 absorption as shown in the bottom panel of Figure 4. Here the Fe II λ2587 optical depth is higher than that of the Fe II λ2600 transition, again opposite from the expected oscillator strengths, which are 0.07 and 0.24, respectively (Erb et al. 2012). The wind scattering emission models of Prochaska et al. (2011) and Scarlata & Panagia (2015) naturally account for these two apparent anomalies, but they also predict prominent fluorescent emission Fe* $\lambda\lambda$2612, 2626 and Mg II emission profiles, as seen in stacked spectra (Erb et al. 2012; Tang et al. 2014; Zhu et al. 2016) and in the individual cases of Rubin et al. (2011) and Martin et al. (2013).

Our MUSE data reveal no signs of fluorescence emission Fe II* $\lambda\lambda$2612, 2626 or Fe II* λ2632, after median-smoothing or summing over large apertures. This absence of direct fluorescent emission signatures in the presence of resonant Fe II and Mg II infilling can be explained by several arguments (Prochaska et al. 2011). First, a large dust opacity ($\tau_{dust} > 10$) would suppress the emission, but this is not consistent with our our low reddening values ($E(B-V) < 0.1$). Second, Prochaska et al. (2011) showed that the emission is suppressed in an anisotropic wind (their Figure 9), where the opening angle θ_w is much smaller than 45°. Lastly, the emission signal may be hidden by the galaxy continuum, and our data lack the required S/N to unveil the emission.

Another potential strong limitation of the Prochaska et al. (2011) and Scarlata & Panagia (2015) models that may explain the absence of fluorescent emission originates in the underlying assumption of a wind velocity that scales linearly with distance $v \propto r^1$. If one relaxes this assumption and instead uses an arctangent wind velocity profile $v(r)$ motivated by the results of Murray et al. (2005, 2011), which has a steep acceleration profile (or a large velocity gradient) inside some turnover radius, the spatial extent of the region of resonance will be much smaller than the scale length of the wind itself. Outside the turnover radius, where the wind velocity is constant with radius, the Sobolev approximation breaks down because $dv/dr \approx 0$, and dust re-absorption may play a much larger role in spite of low reddening values. A full wind scattering model is beyond the scope of this paper.

We now attempt to estimate the mass flux in the wind. In the case of a mass-conserving flow, the mass outflow rate can be estimated using this formula (Heckman et al. 2000, 2015)

$$\dot{M}_{in}(b) \propto \Omega_{out} N_H r_{out} V_{out}, \approx 0.3\ \Omega_{out,2}\ \mu_{1.6}\ N_{H,20.4}\ r_{out,1}\ V_{out,80}\ M_\odot yr^{-1}, \quad (2)$$

where Ω_{out} is the wind solid angle, μ the mean particle weight, N_H the gas column density, r_{out} the launch radius, and V_{out} the wind speed. With blueshifted low-ionization lines in galaxy

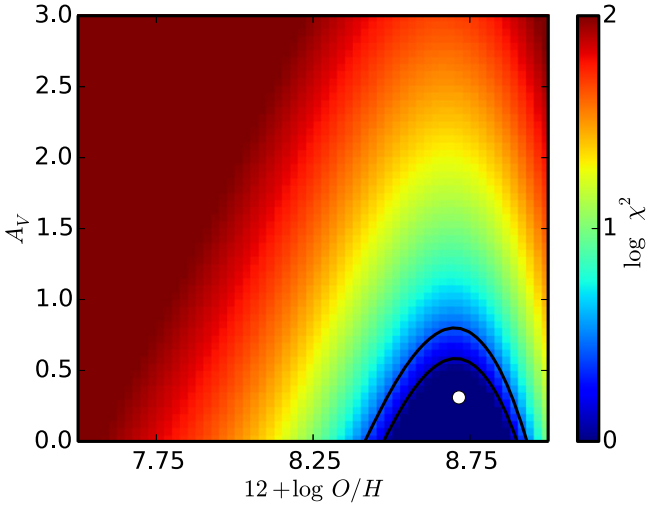

Figure 5. Likelihood contours for the metallicity using the [N II]/Hα and [O II]/Hβ constraints with $E(B-V)$ set to 0.10 determined from the Balmer decrement. The contours show that the metallicity estimate $12+\log \mathrm{O/H} = 8.7 \pm 0.2$ is robust against errors in the extinction estimate, because the [O II]/Hβ ratio is sampling the peak of the relation between [O II]/Hβ and metallicity.

Table 5
Host Galaxy Kinematics

Property	Hα	[O II]	Hβ
Seeing (arcsec)	0.78	0.55	0.55
S/N pixel^{-1} (max)	4.8	45	19
$R_{1/2}$ (kpc)	4.0 ± 0.2	3.9 ± 0.2	2.7 ± 0.3
incl. (°)	57 ± 2	61 ± 2	41 ± 2
P.A. (°)	80 ± 2	71 ± 2	75 ± 3
$V_{\rm max}$ (km s^{-1})[a]	123 ± 5	100 ± 10	105 ± 10
r_t (kpc)	1.5	1.5	1.5
σ_o (km s^{-1})	42 ± 5	34 ± 2	32 ± 3

Note. These morphological and kinematic parameters are determined from our 3D fits using our GalPaK^{3D} algorithm.
[a] With the turnover radius r_t fixed to 1.5 kpc.

spectra, only the wind speed is well constrained. As argued in Bouché et al. (2012) and Schroetter et al. (2015), the launch radius $r_{\rm out}$ is the most uncertain ingredient of Equation (2).

We can estimate the wind speed $V_{\rm out}$ from the blueshifted Mg II absorption in the galaxy spectra. Using a Gaussian fit to the Mg II λ2803 component (or two Gaussians to the doublet), we find a Doppler offset of -45 ± 15 km s^{-1}. However, the Mg II absorption harbors a significant component from the ISM at zero velocity. Hence, performing a double-Gaussian fit to the absorption representing the ISM[18] and the wind components (as in Martin et al. 2012; Kacprzak et al. 2014) shown in Figure 4, we find that the wind speed (at peak optical depth) is about $V_{\rm out} \approx -80 \pm 15$ km s^{-1}. This is the bulk velocity where most of the optical depth is, but the Mg II profile (and the Fe II profile) shows absorption up to ~ -150 km s^{-1}. For a bi-conical flow, this wind speed represents the flow speed along any radial trajectories, but if the absorption originates from regions close to the disk where the flow is more cylindrical, $V_{\rm out}$ ought to be corrected for the galaxy inclination ($\cos i$) and would be -160 km s^{-1} since the galaxy inclination is $\sim$60°.

Following Leitherer et al. (2013), Wood et al. (2015), and Heckman et al. (2015), one can estimate the hydrogen column density using the gas-to-dust ratio and the relationship between $N_{\rm H}$ and reddening (e.g., Bohlin et al. 1978; Diplas & Savage 1994; Ménard & Chelouche 2009),

$$N(\mathrm{H}) = 4.9 \times 10^{21} \times E(B-V)\ \mathrm{cm}^{-2}, \quad (3)$$

which with our estimate of $E(B-V) \sim 0.1$ leads to a total gas column density of $N_{\rm H} \sim 5 \times 10^{20}$ cm^{-2}. As argued in Wood et al. (2015), this value represents an upper limit on the column density, as the extinction traces the column density to the star cluster and thus likely includes contributions from gas in both the disk and the wind. Another lower limit comes from the Mg II rest-frame equivalent width $W_r^{2796} \sim 3.5$ Å (Table 3), which implies a column density $>2 \times 10^{20}$ cm^{-2} from the Ménard & Chelouche (2009) column density–Mg II equivalent width correlation, i.e., at least about 40% of the column density is in the wind.

Regarding the wind solid angle $\Omega_{\rm out}$, we use the now firmly established result that winds appear well collimated (Bordoloi et al. 2011; Bouché et al. 2012; Kacprzak et al. 2012; Martin et al. 2012; Bordoloi et al. 2014; Rubin et al. 2014; Zhu et al. 2014). These constraints on the opening angle $\theta_{\rm out}$ show that it is on average $\approx \pm 30°$. In our galaxy, $\theta_{\rm out}$ cannot be measured directly, although an indirect constraint comes from the emission infill discussed above, which indicates that $\theta_{\rm out}$ is much smaller than 45°. Overall, the total wind solid angle $\Omega_{\rm out}$ is $\approx$2, for both sides of a bi-conical flow, with likely values ranging from 1.7 to 3.9 for $\theta_{\rm out}$ ranging from 30° to 45°.

As mentioned, the launch radius $r_{\rm out}$ is the most uncertain ingredient in Equation (2) from blueshifted absorption lines. Some authors take a fixed value of 5 kpc (e.g., Rupke et al. 2005; Weiner et al. 2009; Chisholm et al. 2015), while others assume $r_{\rm out} = 2 \times R_{1/2}$ (e.g., Heckman et al. 2015). However, it could be 0.5 kpc or 5 kpc, as blueshifted absorption is rather unable to distinguish these possibilities. Here we take the conservative point of view that the wind is launched not far from the disk with $r_{\rm out}$ of 1 kpc, which is the typical thickness for high-redshift galaxies (e.g., Elmegreen & Elmegreen 2006).

With these assumptions, the mass outflow rate $\dot{M}_{\rm out}$ for the wind seen in this galaxy is about $\dot{M}_{\rm out} \approx 0.3\ M_\odot\ \mathrm{yr}^{-1}$. A robust upper limit comes from the maximum allowed range for the column density ($N_{\rm Hmax} = 4.9 \times 10^{21}$ cm^{-2}), $\Omega_{\rm out,max} = 3.9$, and $r_{\rm out,max} = 5$ kpc, and the mass outflow rate $\dot{M}_{\rm out}$ is at most $<6\ M_\odot\ \mathrm{yr}^{-1}$. With the considerable uncertainties in the allowed values for $\theta_{\rm out}$ and $r_{\rm out}$, the mass outflow rate $\dot{M}_{\rm out}$ is most likely between 0.2 and 6 $M_\odot\ \mathrm{yr}^{-1}$.

5. PROPERTIES OF THE CIRCUMGALACTIC MEDIUM

5.1. Line-of-sight Abundances

We now turn to the analysis of the kinematics of the circumgalactic medium (CGM) seen in absorption against the background quasar. From the VLT/UVES high-resolution spectra of the quasar, we constrain the abundances in several elements, including Zn, Fe, Si, Cr, Mn, and Ti. Figure 7 shows each of these elements, and Table 6 summarizes our measurements. We used Carswell's VPFIT program (v9.5; Carswell et al.: http://www.ast.cam.ac.uk/~rfc/vpfit.html) to

[18] Because such a double-Gaussian fit is highly degenerate, we fix the ISM component at $v = 0$ km s^{-1} and set its width to 35 km s^{-1}, a value taken from the nebular line emissions.

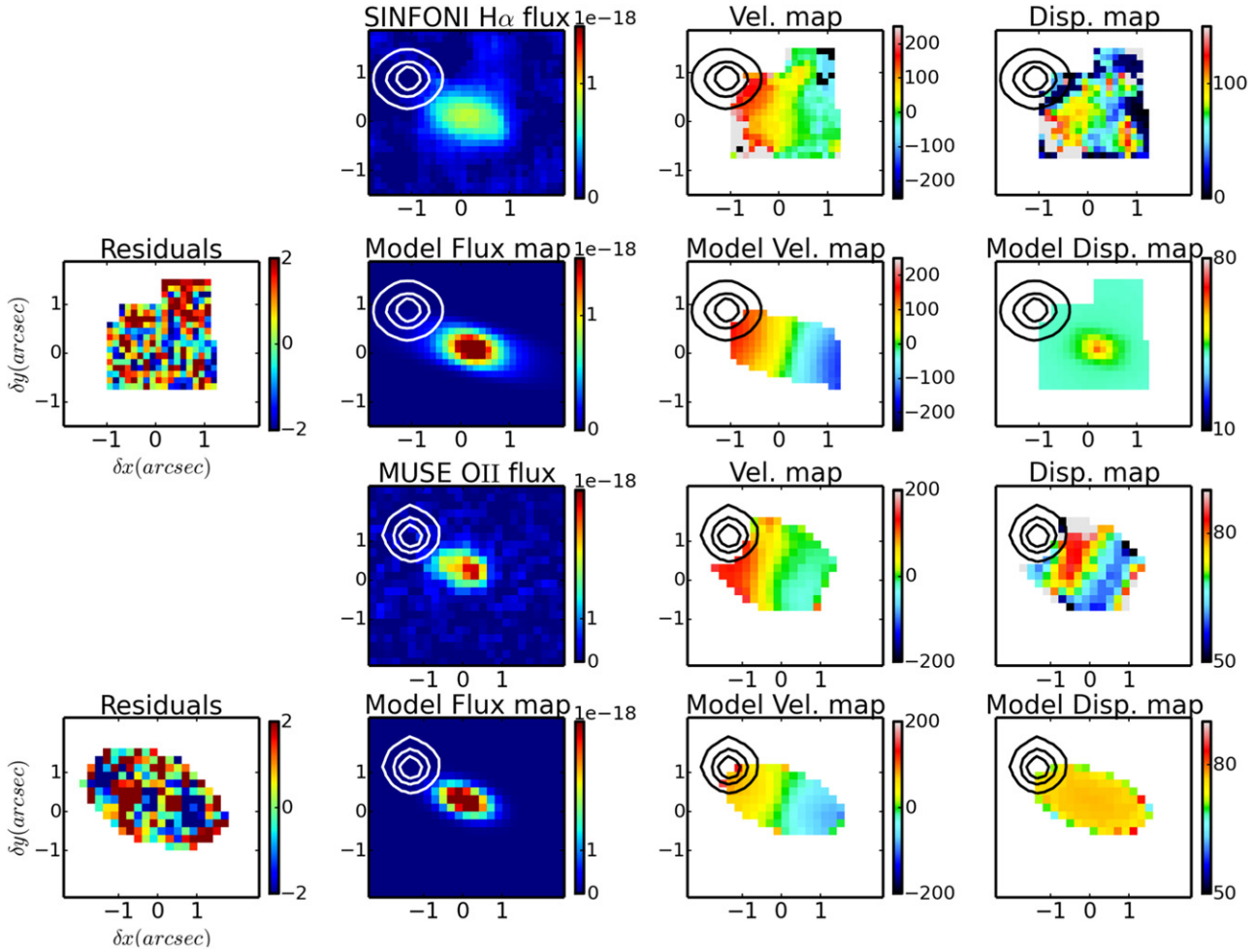

Figure 6. Flux maps and kinematics from the Hα SINFONI (top rows) and the [O II] MUSE data (bottom rows). The first row shows the flux (in erg s^{-1} cm^{-2}), velocity (in km s^{-1}), and dispersion (in km s^{-1}) maps from the Hα SINFONI data (Schroetter et al. 2015). The second row shows the residual map (in units of σ), flux, velocity, and dispersion maps extracted from the 3D forward model (convolved with the PSF) whose parameters are determined using our GalPaK^{3D} algorithm (Bouché et al. 2015). The morpho-kinematics parameters of the model are found using the posterior distribution of the Monte Carlo Markov Chains. The third and fourth rows show the same for the [O II] line. The resulting galaxy models determined from Hα and [O II] are similar (see Table 4). In each panel, the quasar PSF is represented by the solid contours.

perform a joint fit to all of the ions, where components in common between two species have the same redshift and Doppler parameters (b-values), to constrain the total column density in each element N_X.

From our *HST*/COS spectra of the Lyα absorption, we fitted the H I Voigt profile and found the column density constraint to be $\log N_{\rm H\,I}({\rm cm}^{-2}) = 20.4 \pm 0.4$ (Figure 8). Taking the Zn column density and the H I column density from the COS spectra, the absorbing gas metallicity is about $[{\rm Zn/H}] = -0.1 \pm 0.4$, assuming no dust depletion. From the Fe and Zn column densities, we estimate the dust content in the quasar sightline to be at $A_V = 0.07$ using the method proposed by Vladilo et al. (2006).

While Zn is the least depleted element, it may still be depleted onto dust grains. Indeed, Jenkins (2009) showed that in Milky Way interstellar sightlines, the observed ion metallicity $[X/{\rm H}]_{\rm obs}$ of element X (including Zn) can be described with the linear relation $[X/{\rm H}]_{\rm obs} = [X/{\rm H}]_0 + A_X\, F_\star$, between the undepleted metallicity of element X, $[X/H]_0$, the propensity of that element to be depleted onto dust grains A_X, and the depletion level $F_\star$. Jenkins (2009) calibrated the propensity A_X and the zero points $[X/{\rm H}]_0$ such that the depletion level $F_\star$ *usually* ranges from 0 to 1 in local ISM sightlines, although some sightlines have negative values in regions with low gas densities $n({\rm H}) < 10^{-2}\,{\rm cm}^{-3}$, as shown in their Figure 16. With multiple ions of different propensity A_X, this set of linear equations (one for each element) can be solved for a unique metallicity Z and a unique $F_\star$ (Jenkins 2009). Furthermore, in the absence of a measurement of the H column density, one can also fit simultaneously for the depletion factor $F_\star$ and for the total gas plus metal column density $\log N_{\rm H\,I}/{\rm cm}^{-2} + \log Z/Z_\odot$.

Using the Jenkins (2009) approach, Figure 9 shows that a joint fit to the ion abundances (Ti, Cr, Fe, Si, Mn, Zn) including the H I column density of 20.4 (Table 6) yields a metallicity of $\log Z/Z_\odot = -0.38 \pm 0.12$ and a low value of $F_\star = -0.35 \pm 0.12$, which is consistent with the low extinction value.[19] Hence, the gas metallicity probed by the background quasar at $b = 12$ kpc from the galaxy is about

[19] As noted earlier, this negative value for the depletion level occurs in some sightlines in the Milky Way ISM in regions with gas densities $n({\rm H}) < 10^{-2}\,{\rm cm}^{-3}$ lower than the mean of the Milky Way sample.

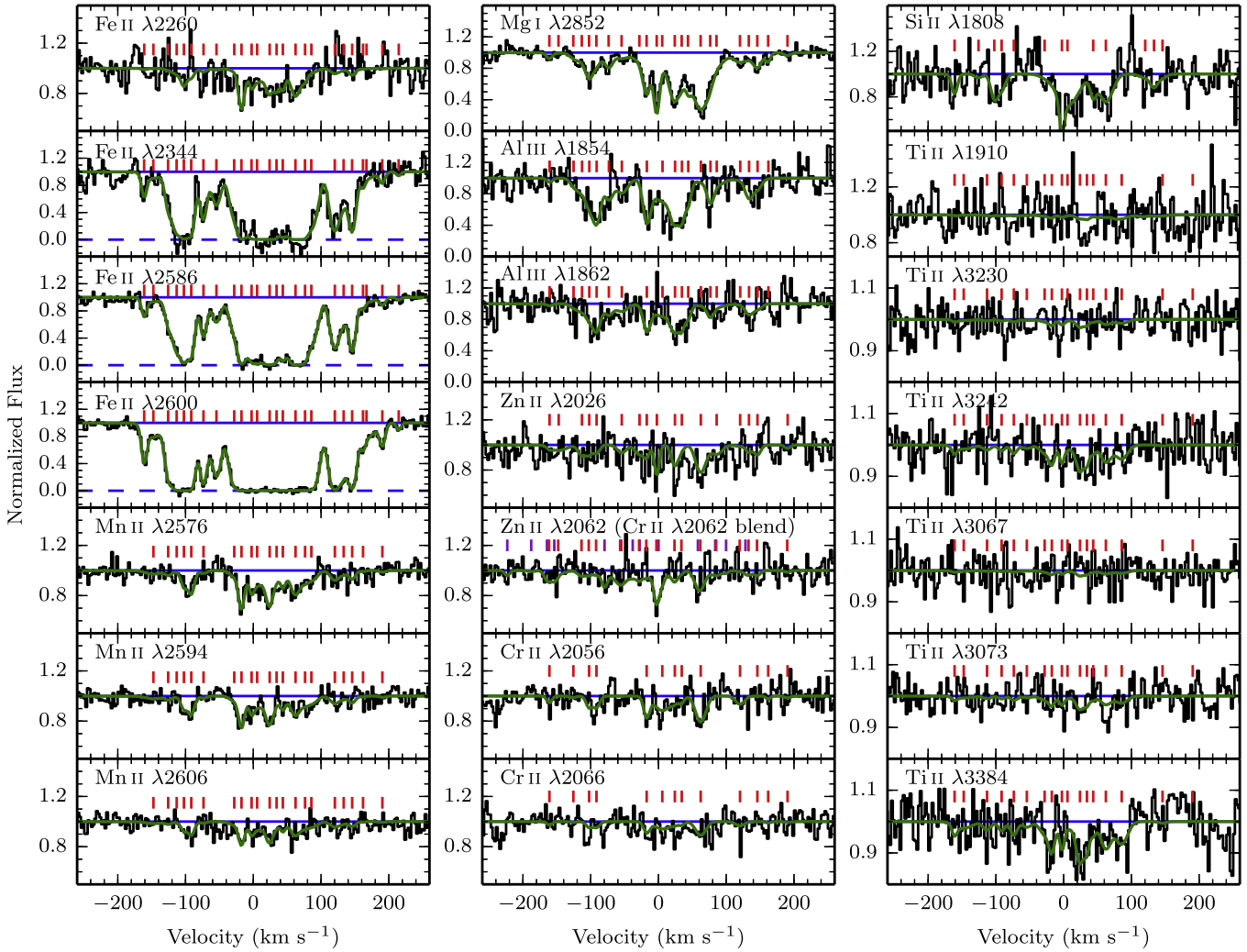

Figure 7. Metal absorption lines detected in the VLT/UVES spectrum toward the background quasar (solid black lines). The fit to the multicomponent absorption system is shown in green for each transition. Red tick marks indicate the position of the individual components. Note that the Zn II λ2062 transition is blended with Cr II λ2062, and tick marks indicating components for Cr II λ2062 are shown in orange. Zero velocity is relative to the galaxy systemic redshift, 0.9096 ± 0.0001.

0.4 $Z_\odot$ (−0.4 dex), albeit with large uncertainties dominated by the uncertainties on the H I column density (0.4 dex).

As discussed earlier, the metallicity of the host from the nebular lines in our MUSE and SINFONI data is about solar (12 + log O/H = 8.7), implying that the metallicity of the gas probed by the quasar line of sight 12 kpc away could be less enriched than that of the host, given the uncertainties. More importantly, the absorbing gas appears to be highly enriched compared to the IGM metallicity of $\log Z/Z_\odot \simeq -2$ or less (e.g., Songaila 2001; Carswell et al. 2002; Schaye et al. 2003; Aguirre et al. 2004, 2008; Simcoe et al. 2004; Pieri et al. 2010, 2014; Shull et al. 2014), which implies that significant mixing must have occurred with recycled gas from past outflows.

5.2. Line-of-sight Kinematics

We now investigate the absorption line-of-sight kinematics using the least saturated low-ionization line Mg I. Figure 10(a) shows the low-ionization Mg I kinematic profile around the systemic velocity for the host redshift $z_{sys} = 0.9096 \pm 0.0001$. The profile clearly shows a strong component at +60–70 km s^{-1}, with other weaker components at intermediate velocities, from −50 to +50 km s^{-1}. There is an additional component at −100 km s^{-1}.

As discussed in the next subsection, we can gain insights into the nature of the absorbing gas by comparing the line-of-sight kinematics (with respect to the host galaxy kinematics) to simple models. Such analyses are powerful, but have only been possible in very few cases, such as in Steidel et al. (2002), Bouché et al. (2012, 2013), Kacprzak et al. (2010, 2014), and Schroetter et al. (2015) with background quasars and in Rubin et al. (2010) and Diamond-Stanic et al. (2015) with a bright background galaxy. This analysis requires good constraints on the galaxy systemic redshift and on the galaxy's relative orientation with respect to the quasar sightline. Fortunately, all of these conditions are met in this study.

5.3. Interpretation of the Line-of-sight Kinematics

The absorption seen in the quasar line of sight shown in Figure 10(a) could arise in the following physical situations:

1. it could be due to the low-ionization component of the outflow (scenario A);

Table 6
UVES Element Abundances

Element	Data/Method	N_X (cm^{-2})	[X/H]
H I	*HST*/COS	20.4 ± 0.4	n.a.
Mg I	VLT/UVES	13.11 ± 0.07	···
Mg II	VLT/UVES	$\geqslant$15.65[a]	$\leqslant -0.3\pm$ 0.4
Fe II	VLT/UVES	15.26 ± 0.03	−0.6 ± 0.4
Si II	VLT/UVES	15.57 ± 0.07	−0.3 ± 0.4
Zn II	VLT/UVES	12.91 ± 0.07	−0.1 ± 0.4
Cr II	VLT/UVES	13.43 ± 0.04	−0.6 ± 0.4
Mn II	VLT/UVES	13.08 ± 0.03	−0.7 ± 0.4
Ti II	VLT/UVES	12.58 ± 0.05	−0.8 ± 0.4
Al III	VLT/UVES	13.53 ± 0.03	···
$\log Z/Z_\odot$	Jenkins09	−0.38 ± 0.12	···
$F_\star$	Jenkins09	−0.35 ± 0.09	···
A_V (mag)	Vladilo06	0.07	···
$E(B-V)$	Vladilo06	0.02	···

Note.
[a] Limit from the Mg II doublet ratio $R \leqslant 1.07$ following Jenkins (1996) and Weiner et al. (2009) given that $W_r^{2796} = 2.8 \pm 0.1$ Å and $W_r^{2803} = 2.6 \pm 0.1$ Å.

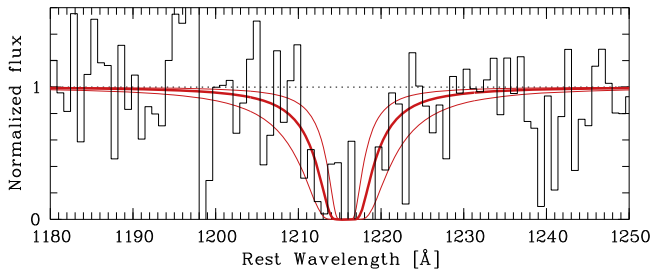

Figure 8. H I profile from an *HST*/COS G230L NUV spectrum, where the best-fit H I column density is found to be $\log N_{\rm H\,I}/{\rm cm}^{-2} = 20.4 \pm 0.4$. The shaded area represents the allowed range in $N_{\rm H\,I}$.

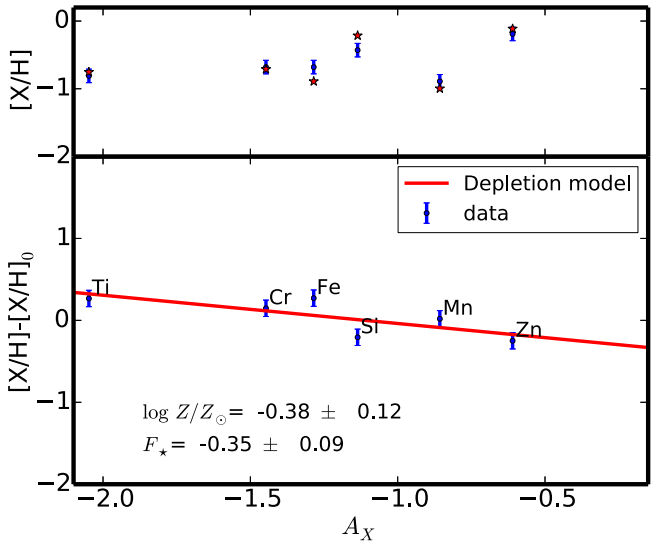

Figure 9. Top: ion abundances for the Zn, Cr, Fe, Ti, and Mn elements present in the QSO UVES spectrum as a function of A_X (the dust propensity factor). Bottom: linear fit to the global metallicity $\log Z/Z_\odot$ where the dust depletion factor $F_\star = -0.35 \pm 0.1$ is given by the slope and $\log Z/Z_\odot = -0.38 \pm 0.12$ is determined from the intercept using the method proposed by Jenkins (2009).

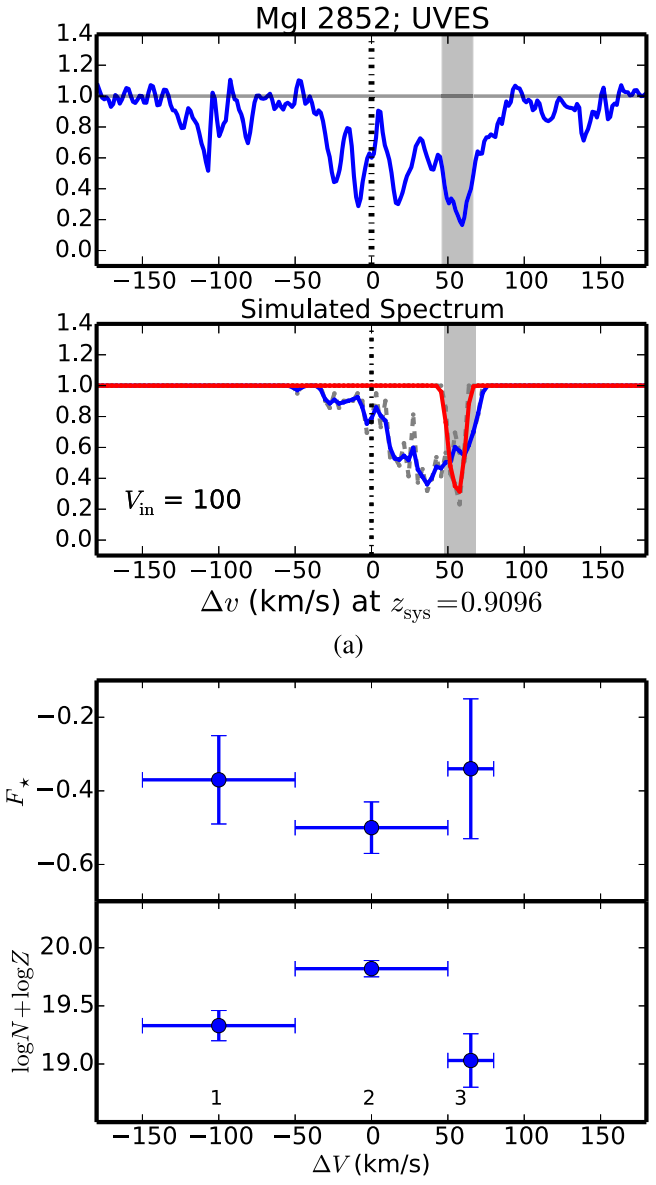

Figure 10. (a) The top panel shows the VLT/UVES spectrum of the Mg I line as a function of the line-of-sight velocity from the systemic redshift $z_{\rm sys} = 0.9096 \pm 0.0001$. The bottom panel shows two simulated profiles (see text), one representing the absorption from a thin disk (red), and the other representing an inflowing model (blue) with $V_{\rm in} = 100$ km s^{-1}. The gray band shows the expected line-of-sight velocity of +65 km s^{-1} at the quasar location determined from the velocity field shown in Figure 11. There is good qualitative agreement between the simulated spectrum and the Mg I profile. (b) The depletion $F_\star$ (top) and the total column density $\log N_{\rm H\,I}/{\rm cm}^{-2} + \log Z/Z_\odot$ (bottom) determined from the Zn II, Cr II, Fe II, Si II, and Mn II column densities in three different zones (labeled 1–3) showing that region 2 has the largest column density and the lowest depletion factor $F_\star$.

2. it could be due to the extended parts of the ISM of the host (scenario B);
3. it could be due to infalling cold gas cooling isotropically from a hot halo (scenario C) akin to high-velocity clouds;
4. it could be due to infalling gas with significant angular momentum forming "cold-flow disks" (scenario D).

An additional scenario often invoked with quasar absorption lines is the invisible satellite possibility. This scenario can never be ruled out in an individual quasar–galaxy pair, but from

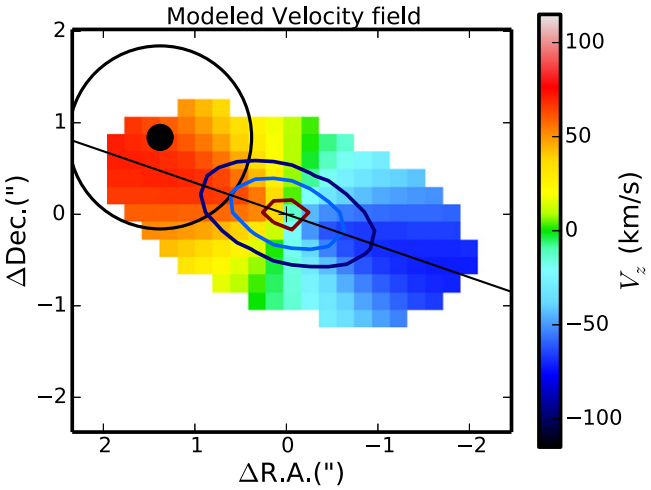

Figure 11. Modeled galaxy velocity field obtained from the VLT/MUSE [O II] data (Figure 6). The contours show the intrinsic flux profile at 50, 150, and 500×10^{-20} erg s^{-1} cm^{-2} arcsec^{-2}. The quasar location at $\Delta\alpha = +1\farcs38$ and $\Delta\delta = +0\farcs84$ is shown by the filled black circle. The circle of radius $r = 1''$ surrounding the quasar is to scale with respect to the circles shown in Figure 2 and its insets.

intervening Mg II statistics, this is the least likely possibility. Indeed, the cross section of satellites is too small to account for the large dN/dz for strong Mg II systems, as argued in Martin (2006).

Before looking at the line-of-sight kinematics, the quasar apparent location does provide tight constraints to distinguish between the three possibilities outlined earlier. Indeed, the quasar apparent position is located at an azimuthal angle of only $\alpha = 15°$ from the galaxy major axis, i.e., the apparent background quasar is almost perfectly aligned with the galaxy's major axis (Figures 2 and 11).

The low azimuthal angle α gives a tight constraint on the outflow scenario "A." In order for the line of sight to intersect a bi-conical outflow, the outflow opening angle $\theta_{\rm out}$ ought to be much larger than $>60°$, i.e., be almost isotropic, given the galaxy inclination $i \sim 60°$. This possibility is not supported by the statistical results in the literature and by our data, as discussed in Section 4.6. Furthermore, a simple bi-conical flow model—which has been successful in reproducing absorption profiles in Bouché et al. (2012), Kacprzak et al. (2014), and Schroetter et al. (2015)—would produce absorption at a single speed because the line of sight is almost entirely radial, and thus it would not account for the velocity range observed in the low-ionization profile shown in Figure 10(a). Hence, we rule out the wind scenario "A."

The low azimuthal angle α also gives a tight constraint on the extended ISM scenario "B," since the projection effects are minimized along the kinematic major axis. Figure 11 shows that, at the quasar location (ΔR.A. $= +1\farcs38$, Δdecl. $= +0\farcs84$), the projected line-of-sight velocity is $V_z = +65$ km s^{-1}, from the modeled intrinsic ("deconvolved") velocity field determined by our 3D fitting algorithm GalPaK^{3D}. Figure 10(a) shows that the maximum optical depth occurs at ~60 km s^{-1}, i.e., is consistent with the extended parts of the ISM velocity field. However, the intermediate-velocity components are not accounted for under this scenario.

We now investigate whether infalling cloud scenarios, with either an isotropic or anisotropic distribution, could account for the intermediate-velocity components at -50 to 50 km s^{-1} in Figure 10(a). Any isotropic distribution for clouds in a galaxy halo would produce symmetric velocity distributions, which is not supported by our data. There are two additional arguments against this isotropic scenario. First, the H I column density is too large ($\log N_{\rm H\,I} = 20.4$ cm^{-2}) compared to the typical column density in high-velocity clouds ($\sim 10^{18}$ cm^{-2}), as discussed in Wakker (2004) and Lehner et al. (2012), and all have $\log N_{\rm H\,I} < 20.2$ (Herenz et al. 2013). Second, our system has an Mg II rest-frame equivalent width of $W_{\rm r}^{2796} \sim 3.5$ Å, whereas the typical high-velocity cloud has a rest-frame equivalent width of $W_{\rm r}^{2796}$ of 0.3–1 Å (Herenz et al. 2013). Lastly, it has been shown by several groups that the strong Mg II systems with $W_{\rm r}^{2796} > 0.8$ Å are not virialized in their host halo (e.g., Bouché et al. 2006; Gauthier et al. 2009; Lundgren et al. 2009).

On the other hand, the intermediate components are qualitatively similar to the features expected for anisotropic gas accretion inside halos. In particular, most numerical hydrosimulations (Dekel et al. 2009; Fumagalli et al. 2011; Stewart et al. 2011a, 2011b; Goerdt et al. 2012; Shen et al. 2013) have shown that accreting material is expected to co-rotate with the central disk in the form of a warped, extended cold gaseous "disk" whose absorption kinematic signatures should follow roughly the rotation direction but offset from the galaxy's systemic velocity (Stewart et al. 2011b). Such rotating gaseous structures are found in the local universe with the large H I disks present around diverse types of galaxies, e.g., around the M81 massive galaxy (Yun et al. 1994), the M33 low surface brightness disk (Putman et al. 2009), and M83 (Huchtmeier & Bohnenstengel 1981; Bigiel et al. 2010), among others. Furthermore, the H I column densities in the outer parts of these systems are well within the range of our observations.

In summary, the intermediate-velocity components of our absorption kinematic profile could be due to an extended cold gaseous "disk" (sometimes referred to as a cold-flow disk), and the largest optical depth component at $V \sim +60$ km s^{-1} is likely due to the extended parts of the galaxy ISM. We now turn toward a more detail modeling analysis of the line-of-sight kinematics.

5.4. Line-of-sight Kinematics Model

In order to assess whether these qualitative signatures are in agreement with the expectations for an extended cold gaseous structure, we used a simple geometrical toy model to generate simulated absorption profiles, as in Bouché et al. (2013). In the model, we distribute "particles" representing gas clouds in a co-planar structure (following the host galaxy's inclination) with predetermined kinematics. The model is composed of two components, one with circular orbits whose velocity is set by the galaxy rotation curve, and one with radial orbits, representing an accretion component. Because the galaxy orientation (galaxy inclination, P.A.) relative to the quasar is well determined from the IFU data, the only free parameter is the inflow speed at the quasar impact parameter ($b = 12$ kpc).

The resulting absorption profile simulated at the UVES resolution is shown in Figure 10(a) and agrees qualitatively with the data. The component resulting from the galaxy's rotation is shown in red, and the component from the radial inflow is shown by the blue line. We found that an inflow speed of ~100 km s^{-1} reproduces the profile shape, except for the component at -100 km s^{-1}, which likely has a separate origin.

We can estimate the gas column density in the intermediate-velocity components using the optical depth profile of the least depleted low-ionization element Zn, or equivalently using the depletion model of Jenkins (2009) on the Zn, Cr, Fe, Si, and Mn column densities measured in three kinematically defined subregions, labeled 1–3 in Figure 10(b). Region "1" is defined from the components at $\Delta V < -50$ km s^{-1}, region "2" is defined around the components at $-50 < \Delta V < 50$ km s^{-1}, and region "3" is defined with $50 < \Delta V < 80$ km s^{-1} corresponding to the galaxy rotation.

Figure 10(b) shows that the depletion factor $F_\star$ and total gas plus metal column density $\log N_{\rm H\,I}/{\rm cm}^{-2} + \log Z/Z_\odot$ are different in the three subregions. The top panel shows that the depletion level seems the lowest in the accretion region (zone 2), consistent with this gas being the least processed. The bottom panel shows that, provided that the metallicity does not vary across the profile significantly, about 70% of the total column density (19.90 of the total 20.05 in $\log N_{\rm H\,I}/{\rm cm}^{-2} + \log Z/Z_\odot$) is carried by the middle zone "2," corresponding to the accretion zone. With a metallicity of -0.4 dex, the gas column density in this zone is then $\log N_{\rm H\,I}/{\rm cm}^{-2} \simeq 20.3$. Note that this 70% fraction is found also using the Zn column density and a uniform metallicity.

With this column density estimate of $\log N_{\rm H\,I}/{\rm cm}^{-2} \simeq 20.2$ and the inflow speed of $V_{\rm in} \approx 100$ km s^{-1}, we can estimate the mass flux rate $\dot{M}_{\rm in}(b)$ in this component from the following arguments following Bouché et al. (2013). For a gaseous structure of thickness h_z and mass density ρ that is intercepted at the quasar impact parameter b, the (radial) accretion flux $\dot{M}_{\rm in}$ through an area of $2\pi b\ h_z$ is

$$\dot{M}_{\rm in}(b) = 2\pi b\ V_{\rm in}\cos(i)\, m_p \mu N_{\rm H}, \quad (4)$$

where i is the inclination of the structure, $N_{\rm H}$ is the total gas column, μ is the mean molecular weight, m_p is the proton mass, and we used the identity $m_p \mu N_{\rm H} = \int dz \rho(b) = \rho(b) h_z/\cos i$.

In our case,

$$\dot{M}_{\rm in}(b) \geqslant 8 \frac{\mu}{1.6} \frac{N_{\rm H}}{10^{20.3}} \frac{b}{12} \frac{V_{\rm in}}{100} \frac{\cos(i)}{0.5}\, M_\odot\ {\rm yr}^{-1}, \quad (5)$$

where $N_{\rm H}$ is the gas column density (cm^{-2}), b the quasar impact parameter (in kpc), $V_{\rm in}$ the inflow velocity (in km s^{-1}), and i the galaxy inclination. Because we are unable to constrain the ionization state of each of the components, this mass flux is strictly a lower limit.

6. DISCUSSIONS

6.1. Accretion Rate

As argued in Section 5.3, the most likely physical interpretation for the intermediate-velocity components in the line-of-sight absorption profile is that of an extended gaseous structure co-planar with the host galaxy similar to several local examples, such as M33, M81, and M83 (Huchtmeier & Bohnenstengel 1981; Yun et al. 1994; Putman et al. 2009; Bigiel et al. 2010). In the previous section, we estimated that the minimum gas accretion rate given by Equation (5) is comparable to the SFR. In this context, it is of interest to compare this estimate to the expected theoretical gas accretion rate. In low-mass galaxies with halo mass below $M_{\rm h} \leqslant 10^{12}$ $M_\odot$, the cooling time is much smaller than the dynamical time (Birnboim & Dekel 2003; Kereš et al. 2005; Dekel & Birnboim 2006), and the maximum theoretical gas accretion rate might be given by the growth rate of the dark matter halo $\dot{M}_{\rm DM}$ times the baryonic fraction f_B modulo an efficiency $\epsilon_{\rm in}$.

Our galaxy toward J1422−00 has a halo mass of $M_{\rm h} \approx 2 \times 10^{11}\, V^3_{\rm max,110}\ M_\odot$, and using the theoretical expectation for the DM accretion rate $\dot{M}_{\rm DM}$ from Genel et al. (2008) or Birnboim et al. (2007), the quantity $f_{\rm B} \times \langle \dot{M}_{\rm DM} \rangle$ is $\approx 4\ M_\odot$, consistent with our accretion rate $\dot{M}_{\rm in}$ estimate. Hence, our mass accretion rate estimate and the maximum theoretical gas accretion rate are comparable, which would imply that the accretion efficiency is near 100%, with the caveat that $\langle \dot{M}_{\rm DM} \rangle$ is a time (or population) averaged quantity, which can have substantial scatter (0.3 dex), while our measurement is an instantaneous quantity.

We can look at the accretion efficiency from the point of view of the steady-state solution of the "bathtub" (Bouché et al. 2010) or "regulator" self-regulator model (Lilly et al. 2013) given that we have simultaneous constraints on accretion and outflow rates. As shown in Bouché et al. (2010) and many others since (Davé et al. 2012; Krumholz et al. 2012; Feldmann 2013, 2015; Lilly et al. 2013; Dekel & Mandelker 2014; Forbes et al. 2014; Peng & Maiolino 2014), galaxies at $z > 4$ can be thought of as a simplified gas regulator where there is a balance between the SFR and the gas accretion rate. The equilibrium solution can be written as

$$\text{SFR} \approx \frac{\epsilon_{\rm in} f_{\rm B}}{1 + R + \eta} \dot{M}_{\rm DM}, \quad (6)$$

where R is the gas returned fraction (from massive stars) under the instantaneous recycling approximation and η the loading factor from stellar feedback. Our galaxy toward J1422−00 has an SFR of $4.7 \pm 2.0\ M_\odot\ {\rm yr}^{-1}$ and a mass outflow rate $M_{\rm out} \approx 0.2$–$6\ M_\odot\ {\rm yr}^{-1}$, yielding a mass loading factor at most unity $\eta \leqslant 1$, and together these numbers imply that $(1 + R + \eta) \times$ SFR is at least (with $\eta = 0$) $> 6\, M_\odot\ {\rm yr}^{-1}$ and at most (with $\eta = 1$) $11\ M_\odot\ {\rm yr}^{-1}$. Together, with the maximum theoretical accretion rate $f_{\rm B} \times \langle \dot{M}_{\rm DM} \rangle \approx 4\ M_\odot$, the accretion efficiency ought to be high, near 100%.

In all, our results indicate that the accretion efficiency is high at $\epsilon_{\rm in} \approx 1.0$, regardless of the loading factor η, in agreement with the theoretical expectation of Dekel & Birnboim (2006) and with the empirical measurements of Behroozi et al. (2013).

6.2. Angular Momentum under the Cold-flow Disk Interpretation

A critical question for these extended gaseous disks is how much angular momentum they carry as discussed in Stewart et al. (2013) and Danovich et al. (2015) compared to that of the disk. We use the common definition of the spin parameter (e.g., Bullock et al. 2001),

$$\lambda \equiv \frac{j}{\sqrt{2}\ R_{\rm vir}\ V_{\rm vir}}, \quad (7)$$

where j is the specific disk angular momentum J/M.

As discussed in Mo et al. (1998), the relation between disk scale length $R_{\rm d}$ and the disk spin λ parameter is $R_{\rm d} \propto \lambda\ R_{\rm vir}\ H(z)^{-1}$, where the proportionality constant depends on the dark matter profile. Using an isothermal profile, we find $\lambda_{\rm gal} = 0.047$ (Equation (12) of Mo et al. 1998). Using a Navarro et al. (1997) (NFW) profile, we estimate $\lambda_{\rm gal}$ to be 0.04–0.05, over a wide range of the disk baryon fraction

(ranging from 0.01 to 0.1). Without direct measurement of the stellar mass, we can use the baryonic Tully–Fisher relation (TFR) to estimate the baryon fraction. Using the baryonic TFR for intermediate-redshifs galaxies (Contini et al. 2015, and references therein), we find that $M_{\rm bar} \approx 5 \times 10^9\ M_\odot$, yielding a baryonic fraction of $M_{\rm bar}/M_{\rm h} = 0.025$, i.e., 2%–3%, a value consistent with the halo-abundance matching techniques (e.g., Moster et al. 2010; Behroozi et al. 2013).

The angular momentum of the cold-flow disk is harder to estimate without a direct size constraint, but we can place useful limits. Since the gas is traced 12 kpc away from the galaxy center, a distance corresponding to three times the half-light radius or $0.15 \times R_{\rm vir}$, assuming the virial relation $R_{\rm vir} \sim 90\ V_{\rm max,110}$ kpc at $z \sim 1$, we find that the gaseous disk carries 50% more angular momentum than that of the galaxy, which has $R = 4$ kpc and $V_{\rm max} = 110$ km s^{-1}. Similarly, the spin parameter of the cold-flow disk $\lambda_{\rm cfd}$ is estimated to be $\lambda_{\rm cfd} > 0.06$ since the ratios between spin parameters and specific angular momenta are identical in a given halo (Equation (7). This limit on the cold-flow disk angular momentum is consistent with the theoretical expectation of Danovich et al. (2015), where the baryons within $0.3\ R_{\rm vir}$ have 2–3 times the galaxy angular momentum.

7. CONCLUSIONS

We presented results on a single quasar–galaxy pair toward the quasar SDSS J142253.31−000149 selected from our SIMPLE survey (Paper I), which consisted of searching for the host galaxies around strong ($W_{\rm r}^{\lambda 2796} > 2$ Å) $z \sim 0.8$–1.0 Mg II absorbers selected from the SDSS database. The background quasar location is 1.″4 away (12 kpc) from the host and is situated about 15° from the galaxy's major axis.

In summary, thanks to our new VLT/MUSE data and our ancillary SINFONI data, we found that the $z_{\rm sys} = 0.9096 \pm 0.0001$ host galaxy of this galaxy–quasar pair

1. is isolated with no neighbors within 240 kpc down to an SFR of 0.22 $M_\odot$ yr^{-1} (5σ), as shown in Figure 2;
2. has a dust-corrected SFR of $4.7 \pm 2.0\ M_\odot$ yr^{-1}, using a Chabrier (2003) IMF, and a small amount of extinction $E(B-V) = 0.1 \pm 0.1$ mag;
3. has a solar metallicity ($12 + \log {\rm O/H} = 8.7 \pm 0.2$) from an analysis of the nebular emission lines detected in MUSE ([O II], Hβ) and SINFONI (Hα), as shown in Figure 5;
4. has a maximum rotation velocity of $V_{\rm max} \simeq 100 \pm 10$ km s^{-1}, corresponding to a halo mass of $M_{\rm h} \simeq 2 \times 10^{11}\ M_\odot$ or to a $0.1\ L_\star$ galaxy, and an inclination of about $i \approx 60°$ simultaneously determined through 3D modeling (Figure 6);
5. has a wind with an estimated mass outflow rate of 0.5–5 $M_\odot$ yr^{-1} (i.e., a loading factor $\eta \leqslant 1$) from the blue-shifted (by $v_{\rm out} = -80 \pm 15$ km s^{-1}) low-ionization absorptions (Mg II and Fe II) in the MUSE galaxy spectrum (Figure 4). The doublet line ratios indicate emission infilling (Prochaska et al. 2011), but the MUSE data do not show fluorescent emission down to $\approx 5 \times 10^{-18}$ erg s^{-1} cm^{-2} arcsec^{-2} (3σ).

In addition, we confirmed the SINFONI results (Paper II; Figure 11) that showed that the quasar is located at an azimuthal angle of $\alpha \approx 15°$ from the galaxy major axis, which makes it very well suited to investigate the presence of extended gaseous structures. The analysis of the quasar absorption profile obtained with the VLT/UVES spectrograph shows

1. distinct signatures of co-planar gas that appears to be co-rotating with the host galaxy, but at a speed lower than the rotation velocity (Figure 10(a)) from the low-ionization metal absorption lines;
2. that the metallicity of the absorping gas is estimated at about $\log Z/Z_\odot = -0.4 \pm 0.4$ ($0.4\ Z_\odot$; Figures 7 and 9) globally across the profile,[20] which is much larger than the IGM metallicity of $\log Z/Z_\odot = -2$ for fresh infalls, implying a significant amount of recycling.

We discussed various interpretations of these absorption signatures (in Section 5.3) and argued that the most likely interpretation is one that is analogous to large H I gas disks seen in the local universe, which can extend 2–3 times larger than the half-light radius. In numerical simulations, such structures can appear at significant look-back times and are sometimes referred to as "cold-flow disks" (Stewart et al. 2011a, 2013). In this context, we estimated that the amount of infalling/accreting material is $\geqslant 8\ M_\odot$ yr^{-1} (Equation (5)), i.e., about two times larger than the SFR. By comparing the estimate of the gas accretion rate and the expected gas inflow rate for a halo of $2 \times 10^{11}\ M_\odot$, we find that the accretion efficiency $\epsilon_{\rm in}$ is $\approx$1.0 for wind loading factors $\eta \leqslant 1$. Finally, we find that the angular momentum of the co-planar structure is at least 50% larger than that of the galaxy given the minimum extent of this structure.

Similar cases appeared recently in the literature. There is our work (Bouché et al. 2013), which showed observational signatures similar to ones presented here in a $z = 2.3$ galaxy, and there are the recent IFU observations of a giant Lyα-emitting filament by Martin et al. (2015) around a high-redshift quasar (Cantalupo et al. 2014), which provide possible evidence for kinematics compatible with a larger (220 kpc in radius) gaseous rotating disk. The similarity between the kinematics of these gaseous structures and those of some hydrodynamical simulations (Stewart et al. 2011a; Shen et al. 2013; Danovich et al. 2015) and the evidence provided in the current study suggest that these structures may not be uncommon in the high-redshift universe.

We thank the anonymous referee for their comments that led to an improved manuscript. We thank E. Emsellem for his insights regarding some of the figures. We thank A. Dekel for his comments on an early version of the draft. This work is based on observations taken at ESO/VLT in Paranal, and we would like to thank the ESO staff for their assistance and support during the MUSE commissioning campaigns. N.B. acknowledges support from a Career Integration Grant (CIG) (PCIG11-GA-2012-321702) within the 7th European Community Framework Program. M.T.M. thanks the Australian Research Council for *Discovery Project* grant DP130100568, which supported this work. J.S. acknowledges support from the European Research Council (ERC) under the European Union's Seventh Framework Program (FP7/2007-2013) / ERC Grant agreement 278594-GasAroundGalaxies. J.R. acknowledges support from the ERC starting grant CALENDS. B.E. acknowledges financial support from "Programme

[20] We are able to constrain the relative metallicity across the absorption profile (Figure 11(b)), but not the absolute metallicity.

National de Cosmologie and Galaxies" (PNCG) of CNRS/INSU, France. Support for program 12522 was provided by NASA through a grant from the Space Telescope Science Institute, which is operated by the Association of Universities for Research in Astronomy, Inc., under NASA contract NAS 5-26555. This work has been carried out thanks to the support of the ANR FOGHAR (ANR-13-BS05-0010-02), the OCEVU Labex (ANR-11-LABX-0060), and the A*MIDEX project (ANR-11-IDEX-0001-02) funded by the "Investissements d'Avenir" French government program managed by the ANR. This research made use of Astropy, a community-developed core PYTHON package for astronomy (Astropy Collaboration et al. 2013), NumPy and SciPy (Oliphant 2007), Matplotlib (Hunter 2007), IPython (Perez& Granger 2007), and NASA's Astrophysics Data System Bibliographic Services.

REFERENCES

Abuter, R., Schreiber, J., Eisenhauer, F., et al. 2006, NewAR, 50, 398
Aguirre, A., Dow-Hygelund, C., Schaye, J., & Theuns, T. 2008, ApJ, 689, 851
Aguirre, A., Schaye, J., Kim, T., et al. 2004, ApJ, 602, 38
Amorisco, N. C., & Bertin, G. 2010, A&A, 519, A47
Asplund, M., Grevesse, N., Sauval, A. J., & Scott, P. 2009, ARA&A, 47, 481
Bacon, R., Accardo, M., Adjali, L., et al. 2010, Proc. SPIE, 7735, 8
Bacon, R., Bauer, S., Böhm, P., et al. 2006, Msngr, 124, 5
Bacon, R., Brinchmann, J., Richard, J., et al. 2015, A&A, 575, A75
Behroozi, P. S., Wechsler, R. H., & Conroy, C. 2013, ApJL, 762, L31
Bigiel, F., Leroy, A., Seibert, M., et al. 2010, ApJL, 720, L31
Birnboim, Y., & Dekel, A. 2003, MNRAS, 345, 349
Birnboim, Y., Dekel, A., & Neistein, E. 2007, MNRAS, 380, 339
Bohlin, R. C., Savage, B. D., & Drake, J. F. 1978, ApJ, 224, 132
Bordoloi, R., Lilly, S. J., Hardmeier, E., et al. 2014, ApJ, 794, 130
Bordoloi, R., Lilly, S. J., Knobel, C., et al. 2011, ApJ, 743, 10
Bouché, N., Carfantan, H., Schroetter, I., Michel-Dansac, L., & Contini, T. 2015, AJ, 150, 92
Bouché, N., Dekel, A., Genzel, R., et al. 2010, ApJ, 718, 1001
Bouché, N., Hohensee, W., Vargas, R., et al. 2012, MNRAS, 426, 801
Bouché, N., Murphy, M. T., Kacprzak, G. G., et al. 2013, Sci, 341, 50
Bouché, N., Murphy, M. T., Péroux, C., et al. 2007, ApJL, 669, L5
Bouché, N., Murphy, M. T., Péroux, C., Csabai, I., & Wild, V. 2006, MNRAS, 371, 495
Bullock, J. S., Dekel, A., Kolatt, T. S., et al. 2001, ApJ, 555, 240
Cantalupo, S., Arrigoni-Battaia, F., Prochaska, J. X., Hennawi, J. F., & Madau, P. 2014, Natur, 506, 63
Carswell, B., Schaye, J., & Kim, T.-S. 2002, ApJ, 578, 43
Chabrier, G. 2003, PASP, 115, 763
Chisholm, J., Tremonti, C. A., Leitherer, C., et al. 2015, ApJ, 811, 43
Contini, T., Epinat, B., Bouché, N., et al. 2015, A&A, submitted (arXiv:astro-ph/1512.00246)
Cresci, G., Hicks, E. K. S., Genzel, R., et al. 2009, ApJ, 697, 115
Crighton, N. H. M., Murphy, M. T., Prochaska, J. X., et al. 2015, MNRAS, 452, 217
Danovich, M., Dekel, A., Hahn, O., Ceverino, D., & Primack, J. 2015, MNRAS, 449, 2087
Danovich, M., Dekel, A., Hahn, O., & Teyssier, R. 2012, MNRAS, 422, 1732
Davé, R., Finlator, K., & Oppenheimer, B. D. 2012, MNRAS, 421, 98
Davies, R. 2007, MNRAS, 375, 1099
Dekel, A., & Birnboim, Y. 2006, MNRAS, 368, 2
Dekel, A., Birnboim, Y., Engel, G., et al. 2009, Natur, 457, 451
Dekel, A., & Mandelker, N. 2014, MNRAS, 444, 2071
Diamond-Stanic, A. M., Coil, A. L., Moustakas, J., et al. 2015, ApJ, submitted (arXiv:astro-ph/1507.01945)
Diplas, A., & Savage, B. D. 1994, ApJ, 427, 274
Elmegreen, B. G., & Elmegreen, D. M. 2006, ApJ, 650, 644
Epinat, B., Tasca, L., Amram, P., et al. 2012, A&A, 539, A92
Erb, D. K., Quider, A. M., Henry, A. L., & Martin, C. L. 2012, ApJ, 759, 26
Feldmann, R. 2013, MNRAS, 433, 1910
Feldmann, R. 2015, MNRAS, 449, 3274
Forbes, J. C., Krumholz, M. R., Burkert, A., & Dekel, A. 2014, MNRAS, 438, 1552
Förster Schreiber, N. M., Genzel, R., Bouché, N., et al. 2009, ApJ, 706, 1364
Freundlich, J., Combes, F., Tacconi, L. J., et al. 2013, A&A, 553, A130
Fumagalli, M., Hennawi, J. F., Prochaska, J. X., et al. 2014, ApJ, 780, 74
Fumagalli, M., Prochaska, J. X., Kasen, D., et al. 2011, MNRAS, 418, 1796
Gauthier, J., Chen, H., & Tinker, J. L. 2009, ApJ, 702, 50
Genel, S., Genzel, R., Bouché, N., et al. 2008, ApJ, 688, 789
Goerdt, T., Dekel, A., Sternberg, A., Gnat, O., & Ceverino, D. 2012, MNRAS, 424, 2292
Heckman, T. M., Alexandroff, R. M., Borthakur, S., Overzier, R., & Leitherer, C. 2015, ApJ, 809, 147
Heckman, T. M., Lehnert, M. D., Strickland, D. K., & Armus, L. 2000, ApJS, 129, 493
Herenz, P., Richter, P., Charlton, J. C., & Masiero, J. R. 2013, A&A, 550, A87
Huchtmeier, W. K., & Bohnenstengel, H.-D. 1981, A&A, 100, 72
Jenkins, E. B. 1996, ApJ, 471, 292
Jenkins, E. B. 2009, ApJ, 700, 1299
Kacprzak, G. G., Churchill, C. W., Ceverino, D., et al. 2010, ApJ, 711, 533
Kacprzak, G. G., Churchill, C. W., & Nielsen, N. M. 2012, ApJL, 760, L7
Kacprzak, G. G., Martin, C. L., Bouché, N., et al. 2014, ApJL, 792, L12
Kaiser, M. E., Hodge, P. E., Keyes, C., et al. 2008, Proc. SPIE, 6, 7014
Kamann, S., Wisotzki, L., & Roth, M. M. 2013, A&A, 549, A71
Kennicutt, R. C. 1998, ARA&A, 36, 189
Kereš, D., Katz, N., Weinberg, D. H., & Davé, R. 2005, MNRAS, 363, 2
Kewley, L. J., Geller, M. J., & Jansen, R. A. 2004, AJ, 127, 2002
Kimm, T., Devriendt, J., Slyz, A., et al. 2011a, arXiv:astro-ph/1106.0538
Kimm, T., Slyz, A., Devriendt, J., & Pichon, C. 2011b, MNRAS, 413, L51
Krumholz, M. R., Dekel, A., & McKee, C. F. 2012, ApJ, 745, 69
Lehner, N., Howk, J. C., Thom, C., et al. 2012, MNRAS, 424, 2896
Leitherer, C., Chandar, R., Tremonti, C. A., Wofford, A., & Schaerer, D. 2013, ApJ, 772, 120
Leroy, A. K., Walter, F., Brinks, E., et al. 2008, AJ, 136, 2782
Lilly, S. J., Carollo, C. M., Pipino, A., Renzini, A., & Peng, Y. 2013, ApJ, 772, 119
Lundgren, B. F., Brunner, R. J., York, D. G., et al. 2009, ApJ, 698, 819
Lynden-Bell, D. 1975, VA, 19, 299
Maiolino, R., Nagao, T., Grazian, A., et al. 2008, A&A, 488, 463
Martin, C. L. 2006, ApJ, 647, 222
Martin, C. L., Shapley, A. E., Coil, A. L., et al. 2012, ApJ, 760, 127
Martin, C. L., Shapley, A. E., Coil, A. L., et al. 2013, ApJ, 770, 41
Martin, D. C., Matuszewski, M., Morrissey, P., et al. 2015, Natur, 524, 192
Ménard, B., & Chelouche, D. 2009, MNRAS, 393, 808
Mo, H. J., Mao, S., & White, S. D. M. 1998, MNRAS, 295, 319
Moster, B. P., Somerville, R. S., Maulbetsch, C., et al. 2010, ApJ, 710, 903
Murray, N., Ménard, B., & Thompson, T. A. 2011, ApJ, 735, 66
Murray, N., Quataert, E., & Thompson, T. A. 2005, ApJ, 618, 569
Navarro, J. F., Frenk, C. S., & White, S. D. M. 1997, ApJ, 490, 493
Noterdaeme, P., Petitjean, P., Carithers, W. C., et al. 2012, A&A, 547, L1
Pagel, B. E. J., & Patchett, B. E. 1975, MNRAS, 172, 13
Peng, Y.-j., & Maiolino, R. 2014, MNRAS, 443, 3643
Pérez-Montero, E. 2014, MNRAS, 441, 2663
Pérez-Montero, E., & Contini, T. 2009, MNRAS, 398, 949
Pérez-Montero, E., Contini, T., Lamareille, F., et al. 2013, A&A, 549, A25
Péroux, C., McMahon, R. G., Storrie-Lombardi, L. J., & Irwin, M. J. 2003, MNRAS, 346, 1103
Pichon, C., Pogosyan, D., Kimm, T., et al. 2011, MNRAS, 418, 2493
Pieri, M. M., Frank, S., Mathur, S., et al. 2010, ApJ, 716, 1084
Pieri, M. M., Mortonson, M. J., Frank, S., et al. 2014, MNRAS, 441, 1718
Prochaska, J. X., Kasen, D., & Rubin, K. 2011, ApJ, 734, 24
Putman, M. E., Peek, J. E. G., Muratov, A., et al. 2009, ApJ, 703, 1486
Rubin, K. H. R., Prochaska, J. X., Koo, D. C., et al. 2014, ApJ, 794, 156
Rubin, K. H. R., Prochaska, J. X., Koo, D. C., & Phillips, A. C. 2012, ApJL, 747, L26
Rubin, K. H. R., Prochaska, J. X., Koo, D. C., Phillips, A. C., & Weiner, B. J. 2010, ApJ, 712, 574
Rubin, K. H. R., Prochaska, J. X., Ménard, B., et al. 2011, ApJ, 728, 55
Rupke, D. S., Veilleux, S., & Sanders, D. B. 2005, ApJS, 160, 115
Saintonge, A., Lutz, D., Genzel, R., et al. 2013, ApJ, 778, 2
Scarlata, C., & Panagia, N. 2015, ApJ, 801, 43
Schaye, J., Aguirre, A., Kim, T., et al. 2003, ApJ, 596, 768
Schmidt, M. 1963, ApJ, 137, 758
Schreiber, J., Thatte, N., Eisenhauer, F., et al. 2004, in ASP Conf. Ser. 314, Astronomical Data Analysis Software and Systems (ADASS) XIII, ed. F. Ochsenbein, M. G. Allen, & D. Egret (San Francisco, CA: ASP), 380
Schroetter, I., Bouché, N., Péroux, C., et al. 2015, ApJ, 804, 83
Shen, S., Madau, P., Guedes, J., et al. 2013, ApJ, 765, 89
Shull, J. M., Danforth, C. W., & Tilton, E. M. 2014, ApJ, 796, 49
Simcoe, R. A., Sargent, W. L. W., & Rauch, M. 2004, ApJ, 606, 92

Sobral, D., Best, P. N., Matsuda, Y., et al. 2012, MNRAS, 420, 1926
Songaila, A. 2001, ApJL, 561, L153
Steidel, C. C., Kollmeier, J. A., Shapley, A. E., et al. 2002, ApJ, 570, 526
Stewart, K. R., Brooks, A. M., Bullock, J. S., et al. 2013, ApJ, 769, 74
Stewart, K. R., Kaufmann, T., Bullock, J. S., et al. 2011a, ApJL, 735, L1
Stewart, K. R., Kaufmann, T., Bullock, J. S., et al. 2011b, ApJ, 738, 39
Tacconi, L. J., Neri, R., Genzel, R., et al. 2013, ApJ, 768, 74
Tang, Y., Giavalisco, M., Guo, Y., & Kurk, J. 2014, ApJ, 793, 92
van de Voort, F., & Schaye, J. 2012, MNRAS, 423, 2991
van den Bergh, S. 1962, AJ, 67, 486
van Dokkum, P. G. 2001, PASP, 113, 1420
Vladilo, G., Centurión, M., Levshakov, S. A., et al. 2006, A&A, 454, 151
Wakker, B. P. 2004, in High Velocity Clouds, Vol. 312, ed. H. van Woerden et al. (Dordrech: Kluwer), 25
Weilbacher, P. M., Streicher, O., Urrutia, T., et al. 2012, Proc. SPIE, 8451, 0
Weiner, B. J., Coil, A. L., Prochaska, J. X., et al. 2009, ApJ, 692, 187
White, S. D. M., & Frenk, C. S. 1991, ApJ, 379, 52
Wood, C. M., Tremonti, C. A., Calzetti, D., et al. 2015, MNRAS, 452, 2712
Yun, M. S., Ho, P. T. P., & Lo, K. Y. 1994, Natur, 372, 530
Zhu, G., Comparat, J., Kneib, J.-P., et al. 2016, ApJ, 815, 48
Zhu, G., Ménard, B., Bizyaev, D., et al. 2014, MNRAS, 439, 3139